

# First Light And Reionisation Epoch Simulations (FLARES) XVI

## Size Evolution of Massive Dusty Galaxies at Cosmic Dawn from UV to IR

Paurush Punyasheel<sup>1,2,3,\*</sup>, Aswin P. Vijayan<sup>1,3,4</sup>, Thomas R. Greve<sup>1,3</sup>, William J. Roper<sup>4</sup>, Hiddo Algera<sup>5,6</sup>, Steven Gillman<sup>1,3</sup>, Bitten Gullberg<sup>1,3</sup>, Dimitrios Irodoutou<sup>7</sup>, Christopher C. Lovell<sup>8</sup>, Louise T. C. Seeyave<sup>4</sup>, Peter A. Thomas<sup>4</sup>, and Stephen M. Wilkins<sup>4</sup>

<sup>1</sup> DTU Space, Technical University of Denmark, Elektrovej 327, DK-2800 Kongens Lyngby, Denmark

<sup>2</sup> Birla Institute of Technology and Science, Sancoale 403726, Goa, India

<sup>3</sup> Cosmic Dawn Center (DAWN)

<sup>4</sup> Astronomy Centre, University of Sussex, Falmer, Brighton BN1 9QH, UK

<sup>5</sup> Hiroshima Astrophysical Science Center, Hiroshima University, 1-3-1 Kagamiyama, Higashi-Hiroshima, Hiroshima 739-8526, Japan

<sup>6</sup> National Astronomical Observatory of Japan, 2-21-1, Osawa, Mitaka, Tokyo, Japan

<sup>7</sup> Department of Physics, University of Helsinki, Gustaf Hällströmin katu 2, FI-00014, Helsinki, Finland

<sup>8</sup> Institute of Cosmology and Gravitation, University of Portsmouth, Burnaby Road, Portsmouth, PO1 3FX, UK

August 21, 2024

### ABSTRACT

We use the First Light And Reionisation Epoch Simulations (FLARES) to study the evolution of the rest-frame ultraviolet (UV) and far-infrared (FIR) sizes for a statistical sample of massive ( $\gtrsim 10^9 M_\odot$ ) high redshift galaxies ( $z \in [5, 10]$ ). Galaxies are post-processed using the SKIRT radiative transfer code, to self-consistently obtain the full spectral energy distribution and surface brightness distribution. We create mock observations of the galaxies for the Near Infrared Camera (NIRCam) to study the rest-frame UV (1500 Å) morphology. We also generate mock rest-frame FIR (50  $\mu\text{m}$ ) photometry and mock ALMA 158  $\mu\text{m}$  (0.01'' – 0.03'' and  $\approx 0.3''$  angular resolution) observations to study the dust-continuum sizes. We find the effect of dust on observed sizes reduces with increasing wavelength from the UV to optical ( $\sim 0.6$  times the UV at 0.4  $\mu\text{m}$ ), with no evolution in FIR sizes. Observed sizes vary within 0.4–1.2 times the intrinsic sizes at different signal to noise ratios (SNR = 5–20) across redshifts. The effect of PSF and noise makes bright structures prominent, whereas fainter regions blend with noise, leading to an underestimation (factor of 0.4 – 0.8) of sizes at SNR=5. At SNR=15–20, the underestimation reduces (factor of 0.6 – 0.9) at  $z = 5 - 8$  but due to PSF, at  $z = 9 - 10$ , bright cores are dominant, resulting in an overestimation (factor of 1.0–1.2) of sizes. For ALMA,  $\approx 0.3''$  resolution sizes are affected by noise which acts as extended emission. The size evolution in UV broadly agrees with current observational samples and other simulations. This work is one of the first to analyse the panchromatic sizes of a statistically significant sample of simulated high-redshift galaxies, complementing a growing body of research highlighting the importance of conducting an equivalent comparison between observed galaxies and their simulated counterparts in the early Universe.

**Key words.** galaxies: photometry – galaxies: evolution – galaxies: high-redshift

## 1. Introduction

Galaxy sizes can provide important insight into the physical processes responsible for galaxy formation and evolution. It is one of the few parameters which can be defined independently by photometry. Sizes in various wavelength ranges across various redshifts can not only tell us about evolution of galaxy properties with time (Conselice 2014), but galaxies of various sizes and morphologies are important to constraint relations like the ultraviolet (UV) luminosity function (Kawamata et al. 2018) by providing completeness measure of data (Marshall et al. 2022). Observations have also shown that sizes of galaxies at fixed stellar mass are smaller at higher redshifts (Franx et al. 2008), hence by studying the galaxy sizes over cosmic time we can study galactic processes affecting the structures of galaxies and thus galaxy evolution. This evolution in galactic processes

can also change the dust and gas content, ultimately affecting the observed morphology. Galaxy mergers, instabilities, gas accretion, gas transport, star formation, and feedback can all affect the sizes of galaxies (Xie et al. 2017). With new high resolution UV and far-IR imaging provided by *JWST* and ALMA, the time is ripe for panchromatic studies of high-redshift galaxies.

At a fixed redshift the relationship between luminosity and size can be expressed as

$$R = R_0 \left( \frac{L_{\text{UV}}}{L_{z=3}^*} \right)^\beta \quad (1)$$

where  $R_0$  is a normalization factor representing the effective radius at  $L_{z=3}^*$ ,  $\beta$ <sup>1</sup> is the slope of this relation, and  $L_{z=3}^*$  is the

\* e-mail: paupun@dtu.dk

e-mail: f20190184@goa.bits-pilani.ac.in

<sup>1</sup>  $\beta$  used here is not equivalent to the UV spectral slope

characteristic rest-frame UV luminosity for  $z \approx 3$  Lyman break galaxies<sup>2</sup>.

Studies (Shibuya et al. 2015; Holwerda et al. 2015; Grazian et al. 2012; Bouwens et al. 2022) also form the base of a growing consensus of a positive  $\beta$  in equation 1. However, the evolution of these values with redshift varies between studies. Shibuya et al. (2015) finds a constant  $\beta = 0.27 \pm 0.01$  and a decreasing  $R_0$  with redshift ( $z < 10$ ). Holwerda et al. (2015) finds  $\beta = 0.24 \pm 0.06$  at  $z \sim 7$  which decreases to  $\beta = 0.12 \pm 0.09$  at  $z \sim 9 - 10$ . Grazian et al. (2012) finds  $\beta = 0.3 - 0.5$  at  $z \sim 7$ . Huang et al. (2013) states  $\beta = 0.22$  at  $z = 4$  and  $\beta = 0.25$  at  $z = 5$ . Recent studies of Hubble Frontier Field lensed galaxies at  $z = 4 - 8$  agrees with a positive and high  $\beta$  ( $\sim 0.4$ ) value (Bouwens et al. 2022). They also show an increasing beta with increasing redshift, but the samples are limited to two bins of  $z = 4$  and  $z = 6 - 8$ , which is insufficient to draw clear conclusions on the evolution of  $\beta$ .

There have also been a number of studies that have explored the size-luminosity relation and the associated physics influencing this relation at these high redshifts, using simulations of galaxy formation and evolution. Studies such as (Liu et al. 2017; Marshall et al. 2019), using semi-analytical models (SAMs) state  $\beta = 0.33$  for  $5 \leq z \leq 10$  galaxies. Many hydrodynamical simulations have also explored the evolution of observed galaxy sizes in the Epoch of Reionisation (EoR). Marshall et al. (2022) studies the size-luminosity relations in the BLUE TIDES simulation (Feng et al. 2016), which shows a decreasing positive  $\beta$  with increasing redshift. Using the SIMBA simulations (Davé et al. 2019), Wu et al. (2020) shows a similar positive  $\beta$  for the FUV sizes. Roper et al. (2022) (hereafter FLARES IV), using the FLARE simulations (Lovell et al. 2021; Vijayan et al. 2021) also shows  $\beta$  in the range of [0.279, 0.319] for redshifts 5 to 8 and  $\beta = 0.519$  for redshift 9.

Galaxy size evolution as a function of redshift can be expressed as

$$R(z) = R_{0,z=0}(1+z)^{-m} \quad (2)$$

where  $R_{0,z=0}$  is a normalization factor corresponding to the size of a galaxy at  $z = 0$  and  $m$  is the slope of the redshift evolution (Mo et al. 1998).  $R_{0,z=0}$  is a free factor.

A number of studies using deep *Hubble Space Telescope* (*HST*) fields have measured the sizes of  $z = 6 - 12$  Lyman-break galaxies (e.g. Oesch et al. 2010; Mosleh et al. 2012; Grazian et al. 2012; Ono et al. 2013; Huang et al. 2013; Holwerda et al. 2015; Kawamata et al. 2015, 2018; Shibuya et al. 2015). These observations find that high-redshift galaxies are small and bright, compared to lower-redshift galaxies, with their half-light radius ( $R_e$ ) in the range of  $0.5 - 1$  kpc at rest-frame wavelength of  $1500 \text{ \AA}$ . These studies report slopes usually in the range  $0.6 \leq m \leq 2.0$  (equation 2), for galaxies with  $L_{UV}$  in the range  $(0.3 - 1)L_{z=3}^*$ .

The size evolution with redshift have also been studied using galaxy simulations studies, such as Liu et al. (2017); Marshall et al. (2019), using SAMs, predicting  $m$  values of  $1.9 - 2.2$  for  $L_{UV}$  in the range  $(0.3 - 1)L_{z=3}^*$ . These values are steeper than most observations, which is accredited to strong supernova feedback in their model which produces a faster evolution of average galaxy sizes at  $z > 5$ , leading to steeper slope when comparing to observations with  $z < 5$ . FLARES (Roper et al. 2022), find  $m$  values of  $1.1 - 1.8$  for  $L_{UV}$  in the range  $(0.3 - 1)L_{z=3}^*$ . These values are consistent with observational studies mentioned above. BLUE TIDES simulations (Marshall et al. 2022) show a size evolution slope  $m = 0.662$ , which is much lower than observations as

<sup>2</sup> This corresponds to  $M_{1600} = -21.0$  mag or  $L_\nu = 10^{29.03} \text{ erg s}^{-1} \text{ Hz}^{-1}$  (Steidel et al. 1999)

well as other simulations, which may be the result of the simulations only running for  $z \geq 7$ , a regime which does not have extreme galaxy growth.

With various studies available, there is no clear consensus on the evolution of  $\beta$  with redshift or  $m$ , in both observational or theoretical studies. It is important to note that there are physical uncertainties in models used in simulations. Conroy & Gunn (2010) discusses substantial uncertainties existing in stellar population synthesis modeling.

The choice of SPS models will effect where a galaxy lies in the luminosity size plane. However, the relative distribution of light in the galaxy will remain the same, leading to no size variation.

Besides this both observational and simulation studies use different galaxy structure definitions as well as resolutions and observing instruments which results in variation of luminosity measurement. Simulations look for gravity bound particles to define a galaxy whereas observations consider objects inside an aperture. This difference in structure definition could also be the reason behind disagreement between observations and simulations in panchromatic studies. Bleeding of light from nearby sources as well as background/dark sources can also play a role in the studies not being in agreement. Using similar analytical methods to compare models and observations becomes really important to constraint physical relations like size-luminosity relation.

A similar analysis of size evolution is considerably harder in the far-infrared (FIR, rest-frame), due to the dust-continuum emission from high redshift galaxies being hard to detect and resolve. Facilities such as ALMA require significant time investment in this regard to achieve meaningful results. Thus there are only a handful of studies that have examined the evolution of sizes in FIR wavelengths at  $z \geq 5$ . Using the ALMA-CRISTAL survey Mitsuhashi et al. (2023) and Ikeda et al. (2024) evaluates the sizes of typical star-forming galaxies at redshifts,  $z = 4 - 6$ , while studying the dust-obscured star formation. They find that dust continuum sizes at  $158 \mu\text{m}$  are approximately 2 times as extended as UV sizes. Similarly Fudamoto et al. (2022) also finds dust continuum and [CII] emission to be extended with sizes larger than FUV sizes. Pozzi et al. (2024) also finds extended dust emission in FIR upto 3 kpc, with the dust continuum sizes bigger by a factor of 2 than the UV sizes. Gullberg et al. (2019) also compared K-band size with  $870 \mu\text{m}$  sizes, finding  $870 \mu\text{m}$  sizes being on average 2.2 times smaller than K-band sizes. These ALMA studies are opposite to the findings of Pop-ping et al. (2022) using the ILLUSTRIS-TNG 50 simulation (Nelson et al. 2019; Pillepich et al. 2019) as well as FLARES IV. They accredit this to clumpy gas distribution around the outskirts of galaxies or massive star-forming clumps within galaxies as major source of UV emission.

Dust in any astrophysical system will impact the radiation travelling through it by the scattering and extinction of photons, and re-emitting them at longer wavelengths. This makes the observed spectra of galaxies very different from the dust-free spectra (Li 2008). The distribution and composition of dust in a galaxy can lead to variability in the amount of dust extinction, decreasing the observed luminosity for dusty regions. The higher the wavelength, the lesser dust affects the radiation (Marshall et al. 2022; Roper et al. 2022). Since size measurement is based on the observed luminosity, this decrease in luminosity caused by dust will also bring variation in the observed size-luminosity or size-redshift evolution relations. Such size variation between mock observations and actual size in simulations has been reported in the THESAN simulations (Shen et al. 2024),

with median intrinsic (no dust) UV sizes being lower than dust attenuated sizes (factor of 1-0.33), with the differences increasing with stellar mass (figure 16 in their paper).

The dust content in the EoR is expected to be less than in the present universe (Li et al. 2019; Vijayan et al. 2019; Magnelli et al. 2020; Pozzi, F. et al. 2021; Yates et al. 2024). However, even small amounts of dust can lead to significant attenuation in the UV. This absorbed energy is re-emitted in the IR, thus studying size evolution in the IR is equally important to understand the dust properties and its evolution in galaxies.

Radiative transfer in astrophysical systems can be simulated to help understand the effect of dust on observed sizes and also galaxy evolution. This work uses the `SKIRT` radiative transfer code (Camps & Baes 2015, 2020) to post-process a sample of galaxies in the FLARES suite of simulations (selection criteria is discussed in section 2.2) and generate their Spectral Energy Distribution (SED) as well as the surface brightness profile in the UV and IR. FLARES is chosen to get a statistical population of massive galaxies ( $\geq 10^9 M_\odot$ ) in the EoR.

We then use the results of this radiation transfer simulation to explore the size-luminosity relation and size evolution of galaxies in the epoch of re-ionisation in UV and FIR regime. We also compare it with a similar analysis in UV, on FLARES galaxies with a Line of Sight (LoS) method (as discussed in Vijayan et al. 2021) in FLARES IV. Costantin et al. (2023) using TNG50, made mock NIRCам observations with `SKIRT` for observed-frame  $2\mu\text{m} - 3.6\mu\text{m}$  at  $3 \leq z \leq 6$  to analyse size evolution. Their study found size evolution slopes of  $m=1.26$  and  $m=1.15$  for F200W and F356W respectively, which are consistent with observational slopes. They also found observed sizes for massive galaxies to be larger than intrinsic stellar mass sizes at lower redshift ( $z=3,4$ ), attributing it to mass being more compact than observable stellar light, predicting heavy dust obscuration.

Such a panchromatic study of galaxy sizes is also very relevant and timely, given the wealth of multi-wavelength data expected in the next decade. With more accurate radiation transfer, disparity between actual sizes to what can be observed by best instruments available to us can also be studied.

The rest of this paper is structured as follows. In Section 2, we detail the FLARES simulations and choices made in `SKIRT` while also detailing the methodology used to make synthetic photometry and mock observations. We also discuss methods of size calculation used. In Section 3 we analyse the galaxy size evolution in UV against redshift, luminosity and mass. We also compare the size disparity between observations and simulations in this section. Section 4 discusses the IR galaxy size evolution with respect to redshift and mass. Section 5 presents a panchromatic analysis between the UV and FIR spectrum sizes. Section 6 expands on the effect of noise and PSF which leads to variation in observation sizes against simulation sizes.

We present our conclusions in Section 7. We use a Planck year 1 cosmology throughout this paper, corresponding to  $\Omega_m = 0.307$ ,  $\Omega_\Lambda = 0.693$ ,  $h = 0.677$ .

## 2. Methodology

### 2.1. The FLARE simulations

The First Light And Reionisation Epoch Simulations (FLARES, Lovell et al. 2021; Vijayan et al. 2021) is a suite of zoom-in simulations of 40 regions chosen from a 3.2 cGpc a side dark matter only box.

These regions were re-simulated until  $z = 4.67$  with full hydrodynamics using the AGNdT9 configuration of the EAGLE

(Schaye et al. 2015; Crain et al. 2015) galaxy formation model (see Table 3 in Schaye et al. 2015). This configuration produces similar stellar mass functions to the reference EAGLE model. This configuration gives more energetic, less frequent AGN feedback events, and better reproduces the gas mass fractions of low mass galaxy groups compared to the reference eagle model.

The regions are selected at  $z = 4.7$  and have a radius of 14 cMpc/h, spanning a wide range of overdensities, from  $\delta = -0.479$  to 0.970 (See Table A1 in Lovell et al. 2021). The simulations were run with a heavily modified version of PGADGET-3 an N-Body Tree-PM smoothed particle hydrodynamics (SPH) code (same as EAGLE, last described in Springel et al. 2005).

The FLARES regions are predominantly biased towards extreme over-density regions within the dark matter simulation box. This choice provides FLARES with a statistically significant sample of massive galaxies in the early Universe, which are expected to be biased to such regions (see Chiang et al. 2013; Lovell et al. 2018). To remove the bias to overdense regions and to ensure a representative sample, a weighting scheme (described in §2.4 in Lovell et al. 2021) is used throughout this paper while calculating mean-median statistics.

### 2.2. Galaxy Selection

A Friends-Of-Friends algorithm (FoF, Davis et al. 1985) is used to find bound groups in the simulations. Amongst these bound groups, galaxies in FLARES are identified with the SUBFIND algorithm (Springel et al. 2001; Dolag et al. 2009). This algorithm finds saddle points in the density field of a FoF halo to identify self-bound substructures. The most bound particle of these structures is denoted as the center of our galaxies. Stellar mass of a galaxy in the simulation is defined based on the star particles present within a 30 physical kpc (pkpc) radius around this center. The same selection criteria as in Vijayan et al. (2022) (hereafter FLARES III) is used to generate our dataset. We only include galaxies with  $>1000$  particles to ensure our sample is well resolved. This is so that the galaxies are well defined physically and also have enough data for Monte Carlo radiative transfer. This selection criteria leaves us with galaxies with stellar mass,  $M_\star > 10^{9.12} M_\odot$  and UV luminosity  $L_{\text{UV},1500\text{\AA}} > 10^{26.9}$  erg/s/Hz. See Table 1 for the detailed distribution amongst mass bins.

### 2.3. SKIRT modelling

In this work we use the `SKIRT` (Camps & Baes 2015, 2020) radiative transfer code to construct rest-frame UV and far-infrared images of the FLARES galaxies. `SKIRT` (Camps & Baes 2015, 2020), is set up to simulate each galaxy in our selection. The setup is the same as described in FLARES III, with a brief description provided here. The SEDs of young stellar populations (age  $\leq 10$  Myr) are modelled using the MAPPINGS III (Groves et al. 2008), while older populations (age  $> 10$  Myr) modelled using the BPASS (Stanway & Eldridge 2018) stellar libraries. We assume a Weingartner & Draine (2001) SMC type dust mixture to simulate dust emission and attenuation effects, with the effect of self absorption by dust taken into account. We take into account the heating of dust by CMB, because at these redshifts ( $z = 5 - 10$ ), the CMB temperatures can be comparable to dust temperatures, affecting the observed luminosities. Furthermore, as all these radiative transfer results are estimated by `SKIRT` using Monte Carlo Method, a higher number of photons simulated would lead to a more accurate result, hence we use  $10^6$  photon packets per each



$z$	Mass Bins ( $M_{\odot}$ )					Total
	$10^9 - 10^{9.5}$	$10^{9.5} - 10^{10}$	$10^{10} - 10^{10.5}$	$10^{10.5} - 10^{11}$	$10^{11} - 10^{11.5}$	
5	1384	1433	830	185	12	3844
6	688	729	300	54	1	1772
7	333	329	100	11	0	773
8	172	134	24	1	0	331
9	78	40	7	1	0	126
10	32	9	3	0	0	44
<b>Total</b>	2184	2555	1667	456	28	6890

**Table 1.** Distribution of galaxies across different redshifts and mass bins

radiation field wavelength grid (Appendix A in *FLARES III* shows how increasing the photon count has negligible effect the accuracy of the radiative transfer results). Other factors such as the distribution of sources, dust and gas along with dust mass fraction are defined for each galaxy based on the *FLARES* star and gas particle data, similar to *FLARES III*.

The observational instruments in *SKIRT* are setup at a distance of 1 Mpc from the galaxy and they have a field of view of  $60 \times 60$  pkpc<sup>2</sup>. This whole field of view is captured in a  $400 \times 400$  pixels frame (this corresponds to a per pixel resolution of 0.023", 0.026", 0.028", 0.030", 0.033", 0.035" for redshifts 5 through 10 respectively). The plane on which these galaxies are observed is the same and hence the orientation of the galaxies in *FLARES*, automatically leads to different viewing angles.

Only at the highest redshifts ( $z \geq 9$ ) corresponding to the most massive galaxies ( $M_{\star} \geq 10^{10} M_{\odot}$ ), where there is a dearth in the number of galaxies sampled in *FLARES* (see Table 1) and corresponds to a high disc galaxy fraction (see *Ferreira et al. 2023*), there will be an increased effect of viewing angle (face-on/edge-on). Based on these parameters, we get a per pixel SED for both UV and IR spectrum as well as the SED for the range [0.08, 1500]  $\mu\text{m}$  for the whole FOV.

The images are centered on each galaxy's centre of potential as provided by *SUBFIND*.

#### 2.4. Comparison with Line of Sight method

While in this work we employ *SKIRT* to produce synthetic images in most previous *FLARES* work we have adopted a simpler approach to produce synthetic observations, including spectra and images. Line of Sight (LoS, as discussed in *Vijayan et al. 2021*) method calculates the effect of dust attenuation by calculating the intervening column density of dust. This is converted to an optical depth measure by assuming a dust extinction curve.

Anisotropic scattering by the dust couples all lines of sight, and dust absorption/emission couples all wavelengths, making the radiative transfer equation highly non-local and nonlinear (*Steinacker et al. 2013*), which is not taken into account in the LoS method, because of its complexity. However, the star-dust geometry is preserved. Radiative transfer using Monte Carlo simulation estimate these effects in both absorption and scattering by dust grains, and can self-consistently generate the dust emission in the IR, which is the major motivation for using *SKIRT* outputs in this study. Figure 1 which plots the radiative transfer luminosities which are  $\approx 0.2 - 0.3$  dex lower than plotted LoS luminosities and shows the added effects which are not accounted for in LoS but also bring a variation in luminosities observed using both methods. Also, in the LoS method, the free parameters that are used to calculate the dust attenuation were chosen to match the UV luminosity function at  $z = 5$  (see Section 2.4 in *Vijayan et al. 2021*). This difference in method of calculating the

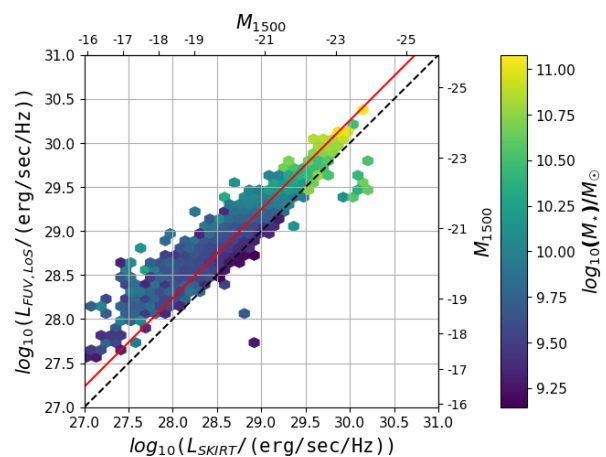


**Fig. 1.** FUV luminosity from *SKIRT* radiative transfer on x axis is compared with LoS luminosities (as discussed in *Vijayan et al. 2021*) on y axis. Luminosity from the LoS method are roughly 0.25-0.3 dex higher than luminosities produced by radiative transfer. The red line is the best fit offset between the two luminosities

dust attenuated luminosity will cause the intercept and slopes of the size-luminosity relation to differ in the two methods. Section 3.2 shows this difference aptly when compared with slopes and intercepts found in the Appendix B of *FLARES IV*.

#### 2.5. Size calculation

Generally to measure sizes, observational studies use either Sérsic profile fitting (*Sérsic 1963*) or a curve of growth method (*Stetson 1990; Ferguson et al. 2004; Bouwens et al. 2004; Oesch et al. 2010*) based on circular or elliptical apertures. Sérsic profile fitting causes variation in sizes compared to the curves of growth sizes in case of a clumpy nature of high redshift galaxies (*Jiang et al. 2013; Bowler et al. 2022*). Clumpy galaxies are elongated in nature with multiple separated bright parts affecting the size calculated. In these galaxies with various bright parts, center selection plays an important role in the half light radius calculation. In simulations, particle distributions can also be used to find the radius enclosing half of the light or mass to determine sizes. Since our aim is to simulate observations and calculate their disparity with observed sizes we use circular apertures, which has been widely used in previous studies (*Bouwens et al. 2004; Oesch et al. 2010*) and use curves of growth (luminosity contained inside a radius) to define our half-light radius. We use two different methods to do so which are described below. Previous *FLARES* work (*FLARES IV*) have used a non parametric pixel based method (e.g. *Bowler et al. 2017*) to calculate sizes. A comparison of the two methods is

also presented below.

### Iterative Aperture Method

We calculate the total luminosity in the galaxy image by summing all pixels within the FoV. For calculating sizes (half light radius) using the Iterative Aperture method, we start with the potential center of the galaxy. We then define a circular aperture of a given radius  $R$  (starting with  $R=0$ ) from the potential centre, and in each iteration calculate the total luminosity inside the aperture. In each iteration we keep increasing  $R$  by 1 pixel until the flux inside the aperture exceeds the 3/4th the total luminosity of the image. Then using the radius values and their corresponding luminosity we interpolate the half light radius (radius with half the total luminosity of the image). We then convert the interpolated values to pkpc by multiplying it with pixel length.

### STATMORPH

`statmorph`<sup>3</sup> (Rodríguez-Gomez et al. 2019) is an open source python package which segments an image to look for objects and calculates their morphological properties. It provides the center of the object, its radius at various light fractions, concentration, asymmetry, clumpiness and Gini-M20 statistics. In this study we use `statmorph` on our mock images to get morphological properties for the galaxies if they were observed.

### Comparison with Pixel Method

`FLARES IV` uses a non parametric pixel approach to calculate the half-light radius. In this method the pixels of the image are ordered from most luminous to least luminous, and then the pixel area containing half the total luminosity is taken into account to calculate the half-light radius assuming a circular aperture. This method is used to account for the clumpy nature of galaxies at high redshift. As this method gives the radius assuming the most compact morphology possible, the sizes calculated by our curves of growth method using circular aperture are higher as they are dependent on structure, clearly seen in Figure 2 which plots the sizes from pixel method against the sizes from curves of growth method for 1500 Å.

It is important to note that for a direct comparison between `FLARES IV`, resolution also plays a role, as contrary to using a spatial resolution of the simulation, this study uses *JWST* resolutions.

## 2.6. Photometry/Image Creation

### 2.6.1. NIRCcam

For generating our mock observations we use a rest-frame wavelength of 1500 Å, corresponding to the far-UV. We make mock observations for *JWST* NIRCcam's filters: F090W, F115W, F140M, F150W, F162M, depending on the redshift.

In the wavelength range of 0.6–2.3 μm observations, the NIRCcam resolution is 0.031"/pixel.

Using the field of view from `skirt` and distance (i.e. redshift) we regridded the images produced from `skirt` to the NIRCcam resolution (see Table A.1).

To mock the observational effects of NIRCcam observations, the images were convolved with a Point Spread Function (PSF) for different filters corresponding to the observed (redshifted) wavelength. We used the PSFs from *JWST* PSF simulation library, simulated by WebbPSF (Perrin et al. 2012, 2014), pro-

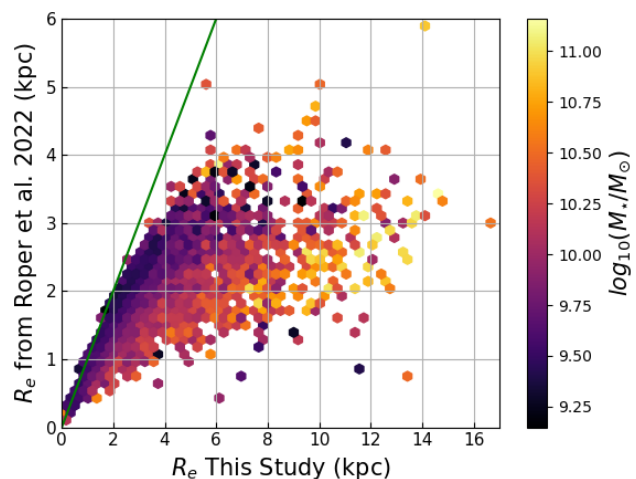


**Fig. 2.** Comparison of the half-light radii at 1500 Å using the method from Roper et al. (2022) and this studies' circular aperture method is shown above. The calculated HLR from a non parametric pixel based method is plotted on the y-axis with the curves of growth inherent size plotted on the x-axis. Sizes from pixel method are lower than curves of growth sizes due to pixel method accounting for the most compact configuration of the galaxy. The green line shows the 1:1 relation

vided by STScI. To the convolved images we added shot/Poisson noise. Due to high number of photons simulated by `skirt`, the number of electrons recorded by each pixel would be very high making the effect of Poisson noise almost negligible. To account for background noise sources the images were further modified with Gaussian noise. To analyse the effect of noise mathematically, noisy mock image was generated uniquely for each source at different SNRs (5–20). Figure 3 shows the evolution of image through various stages described above and Figure 4 shows a sample of NIRCcam RGB false color images (F200W, F150W, F115W) for galaxies in different mass bins. We then evaluated results at Signal to Noise Ratios (SNR) of 5, 10, 15, and 20 (corresponding to exposure times of approximately 5, 14, 40, 70 minutes at  $z = 5$  for an observations similar to CEERS (Holwerda et al. 2024) for a representative galaxy with NIRCcam (F090W) flux, to see the effect of observation time on the observed sizes.

We use `detect_sources` from the `photutils` (Bradley et al. 2023) library to create a segmentation map (sources are defined with  $1.5 \sigma$  detection and a criteria of 5 minimum connected pixels). Depending on the background SNR added to the image, our segmentation maps can differ (see Figure 3). This effect is significant at lower SNRs. The segmentation algorithm which takes into account the minimum number of connected pixels for an object, hence can identify two or more objects from a single galaxy image. In these cases we considered the brightest source as our galaxy. We also evaluated our galaxies, by simulating observations for being a part of a large survey with each galaxy embedded in a Gaussian noise field with a fixed standard deviation for all the sources. The effect of such an analysis is present in Appendix E. For all further analysis results of SNR=5 are used.

### 2.6.2. Far-IR photometry

We produce per pixel SED data for the far-infrared from our radiative transfer simulations. We use this data to analyse sizes in IR using the same methods described above. At these high-redshifts, there are no similar observatories (without unrealistic

<sup>3</sup> <https://statmorph.readthedocs.io>

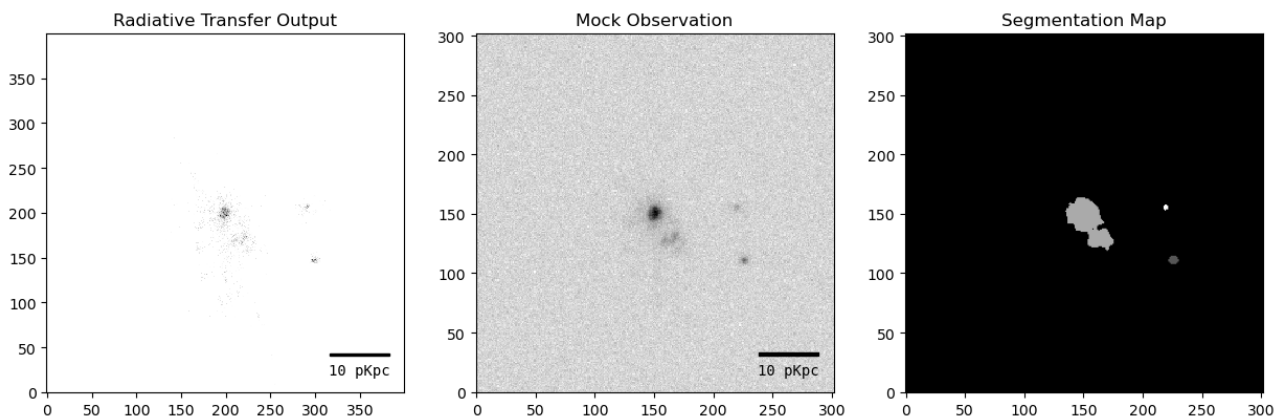


**Fig. 3.** The panes show image of a sample galaxy at  $z = 5$  at various stages of methodology, in a  $60 \times 60$  pkpc<sup>2</sup> field of view. **Left:** The result of `skirt` radiative transfer simulation. **Middle:** Mock observation produced after regridding to  $302 \times 302$  pixels based on NIRCam resolution at this redshift and adding the effects of Gaussian + shot noise corresponding to  $\text{SNR}=10$  and PSF. **Right:** Image shows the segmentation map generated for this image with three distinct objects detected

observational time required) with as high a resolution as *JWST* in the rest-frame IR (the highest resolution channel on the *Herschel Space Observatory* was 5 arcsec),

we create an arbitrary PSF from a 2D Gaussian kernel with a standard deviation of 2 pixels ( $0.062''$ , this is the same as NIRCam resolution for FUV) for adding observational effects to our images. Gaussian and shot noise are also added. We do this process for the wavelengths of  $50 \mu\text{m}$  and  $250 \mu\text{m}$ . There is no significant sizes evolution for our sample as shown in Section 4.3, and hence we use the  $50 \mu\text{m}$  mock photometry for all further analysis.

### 2.6.3. ALMA Simulations

We simulate ALMA images for rest frame dust continuum surrounding ( $158 \mu\text{m}$ ). We use `simobserve` task in CASA (CASA Team et al. 2022), to create the measurement set. We simulate ALMA observations with two different methods described below:

- *High angular resolution*: We simulate observations with  $\approx 0.02''$  angular resolution hence requiring the extended C-8 configuration. The resultant images produced (for the same sample of galaxies as in Figure 4) are shown in Figure F.1.
- *Low angular resolution*: We also simulate observations with similar parameters as presented in the CRISTAL survey (Mitsuhashi et al. 2023). We use configuration C3 for ALMA, which leads to a resolution of  $\approx 0.3''$ . The resultant images are shown in Figure 5.

For both these categories, observation are done with a bandwidth of 7.5 GHz around the red-shifted frequency (rest-frame  $158 \mu\text{m}$ ) for our observations, using pre-induced noise ( $\text{SNR}=10$ ) in the radiative transfer output, simulated for beam effect produced by ALMA. We set a sky temperature of 260K for the simulation with the zenith opacity being 0.1 at the observing frequency. To analyse the simulated observations we clean the obtained output by running `Tclean`, the inherent cleaning algorithm in CASA, for 10000 iterations, deconvoluting the data using Hogbom CLEAN algorithm (Högbom 1974). The maximum and minimum depth of cleaning are 0.05 and 0.8 times the PSF fraction respectively.

## 3. UV Size Analysis

In this section we analyse how the UV sizes evolve with cosmic time, luminosity, mass and also wavelength. We compare sizes in our study with prominent observational and simulation studies. We also analyse the variation of galaxy sizes at  $1500 \text{ \AA}$  between simulations and mock observations.

### 3.1. Observation vs Simulation Sizes

Mock observations using simulations have shown stark difference between observed and intrinsic size evolution relations. Galaxies in the `BLUETIDES` simulation (Marshall et al. 2022) show a negative intrinsic size luminosity relation at  $z=7$ , which when evaluated for dust attenuation results in a positive relations. Similarly in `FLARES (FLARES IV)` negative intrinsic size stellar mass and intrinsic size luminosity relations also show a positive correlation for dust attenuation. Although the `SIMBA` simulations (Davé et al. 2019), uniquely shows positive correlation for intrinsic and observed size with mass (Wu et al. 2020). Similar to the above studies, we compare variation between mock observational sizes and simulational sizes to analyse the observational effects causing the variation in size evolution relations. Figure 6 compares the sizes from mock observations and radiative transfer intrinsic sizes for each of the redshift (0.40-1.16 times). The figure shows a significant variation in observations and simulation sizes. From the figure it can be clearly seen that observational sizes will be underestimated (0.40-0.94 times) for all redshifts for  $\text{SNR} \leq 10$ . For higher SNRs for lower redshift ( $z \in [5, 6, 7, 8]$ ) sizes will be underestimated (0.64-0.83 times) while the sizes for higher redshift ( $z \in [9, 10]$ ) will be slightly overestimated (1.04-1.16 times) compared to actual sizes. Details of overestimation and underestimation with respect to SNRs is present in Table 2. `THE SAN` simulations (Shen et al. 2024) also shows a similar variation in size with galaxies with  $10^7 > M_*/M_\odot > 10^9$  having median simulation size being greater than upto 3 times the observed sizes with increasing stellar mass. This variation in sizes is primarily due to observational effects (PSF and noise) as the offset is independent of galaxy properties like stellar mass and FUV luminosities (see Figure C.1). Only at high luminosities ( $L > 10^{29} \text{ erg/sec/Hz}$ ) where observational effects fail to efficiently wash out fainter regions of the galaxy in



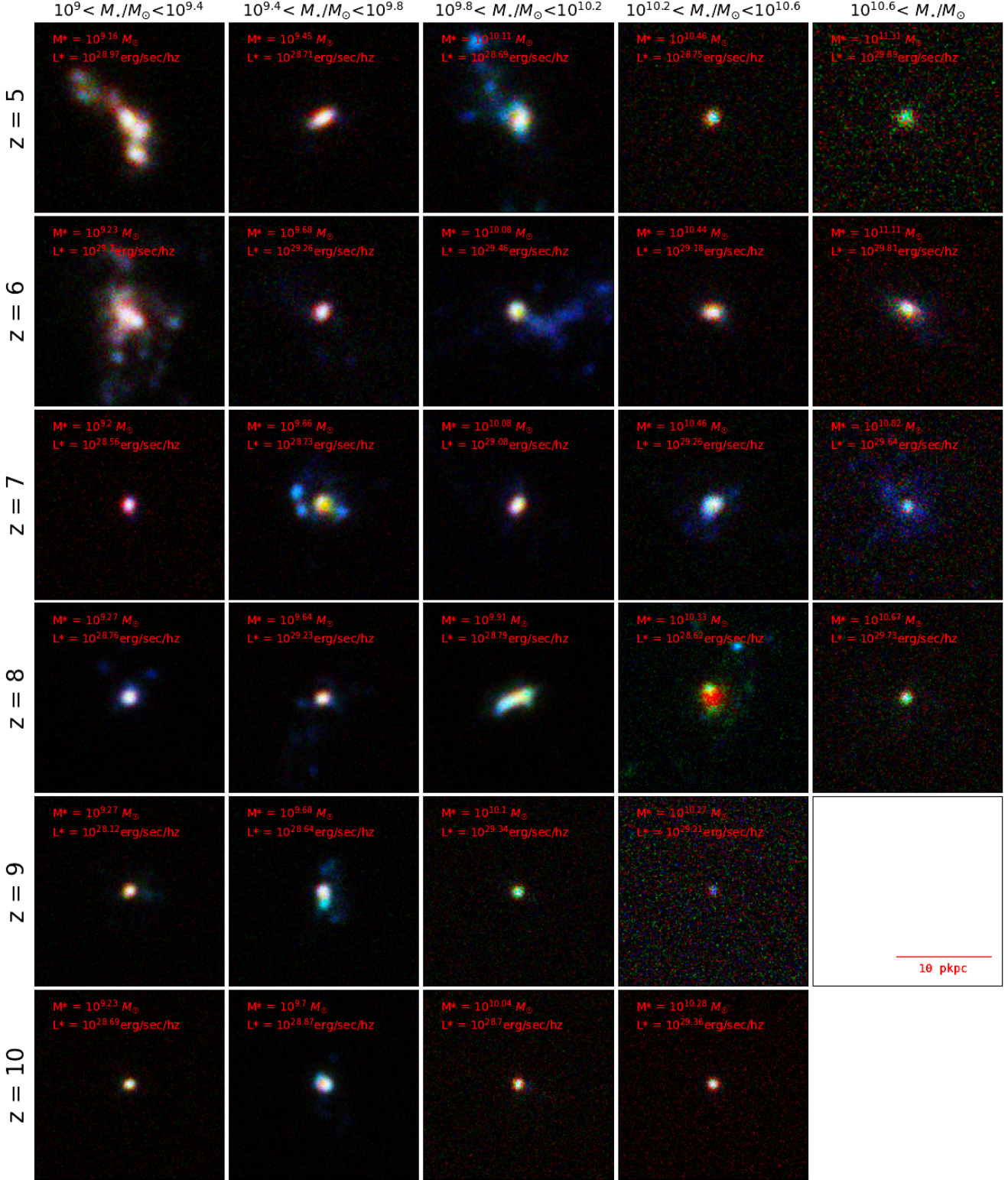


**Fig. 4.** The above false color images show sample galaxies at different redshifts and various mass bins at SNR=20. The field-of-view of the images is 20pkpc and the red, green and blue channel taken from JWST/NIRCam F200W, F150W, F115W filter data respectively.

imaging (further explanation is present in Section 6) size ratio is seen tending to 1.

Sizes from mock images are calculated by STATMORPH, while as center of potential is known to us from simulation, we calculate the simulation sizes using the Iterative Aperture Method (as discussed in Section 2.5). Similar to Figure 6 slope of the best

fit lines for the mock image sizes to simulation sizes for different signal to noise ratios is presented in Table 2. With the effect of noise decreasing with increasing SNR at high-redshift we see that most sizes are overestimated. Noise being primarily responsible for washing away fainter parts of the galaxy along with the PSF intensifying the bright parts of the galaxy, this effect with



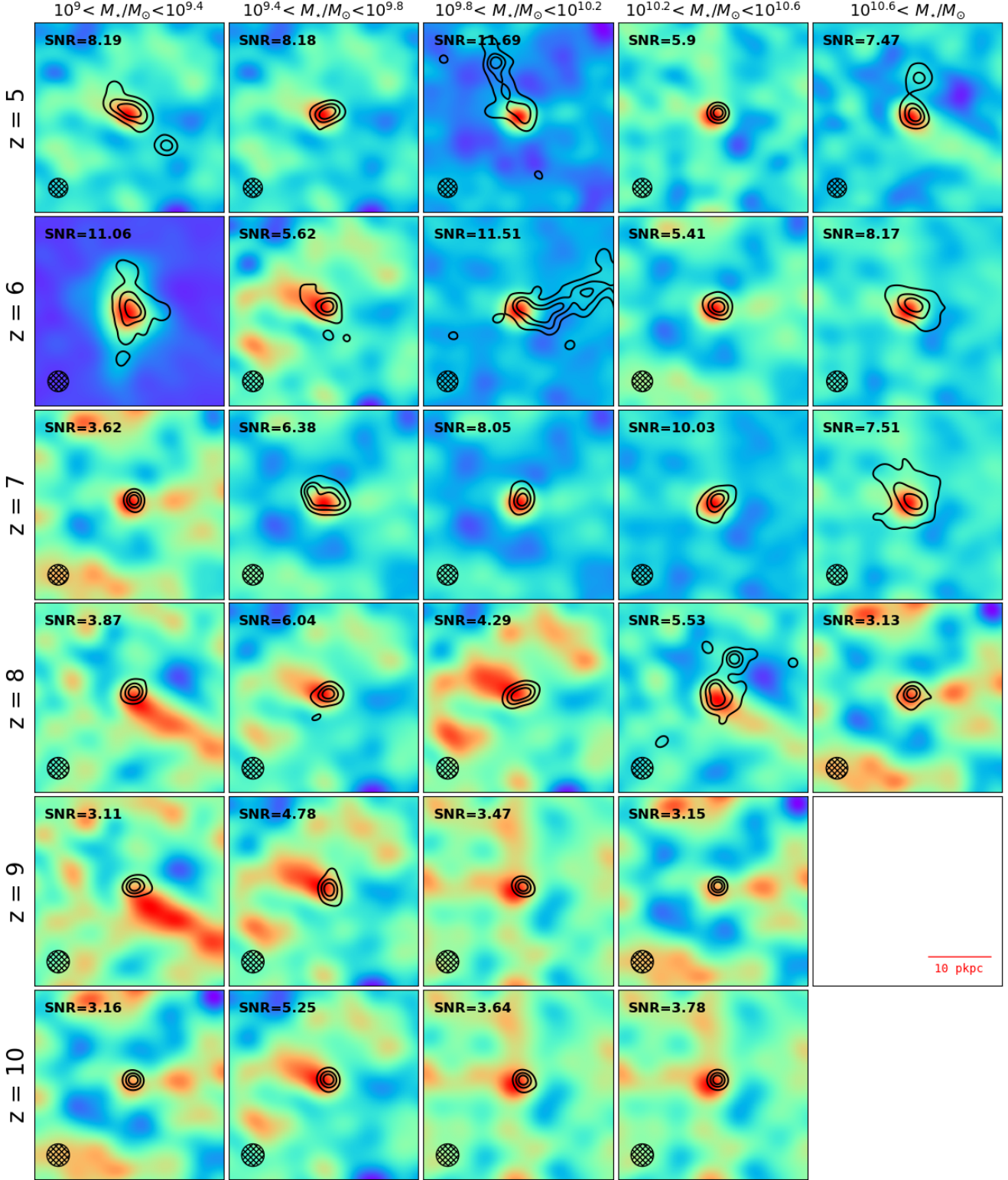


**Fig. 5.** The figure shows the sample of galaxies (same galaxies as in Figure 4) as observed by ALMA at 158  $\mu\text{m}$  at an aperture of 30 pkpc. Low angular resolution ( $\approx 0.1''$ ) (similar to CRISTAL program) is used. The beam size is shown by the circle at bottom left corner. The black contours show 4 linearly spaced contours between brightest pixel to 1/4th of brightest pixel for 1500  $\text{\AA}$ .

increasing SNR shows the difficulty accounting for the complex PSF which causes overestimated sizes (see Section 6).

### 3.2. Size-Luminosity relation

We binned our data in luminosity bins of 0.3 dex and calculated the median luminosity and median sizes in these bins. We fit Equation 1 to these medians. Figure 7 shows a luminosity-size fit for our sample across different redshifts compared to obser-



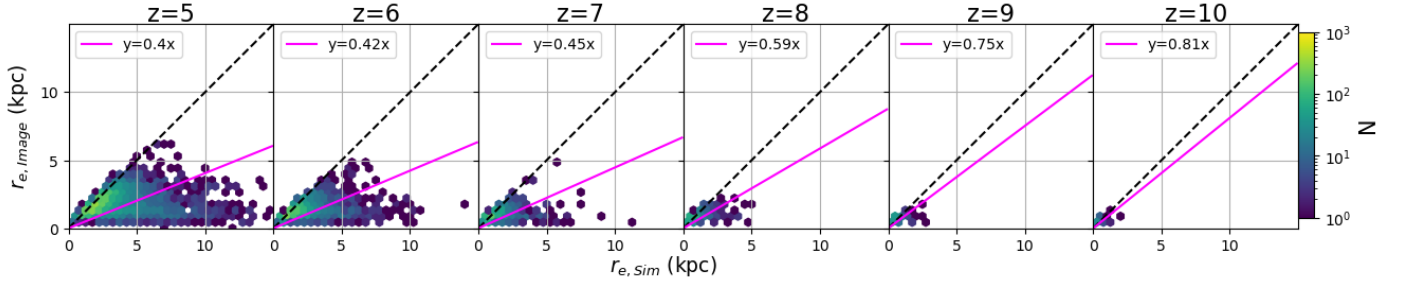


**Fig. 6.** UV sizes of mock images (y-axis) are plotted as a function of sizes directly from radiative transfer (x-axis) at SNR=5. The black dashed line is a 1:1 relation whereas the yellow line is the best fit  $y=mx$  relation where  $y$  is mock image effective radius and  $x$  is simulation effective radius

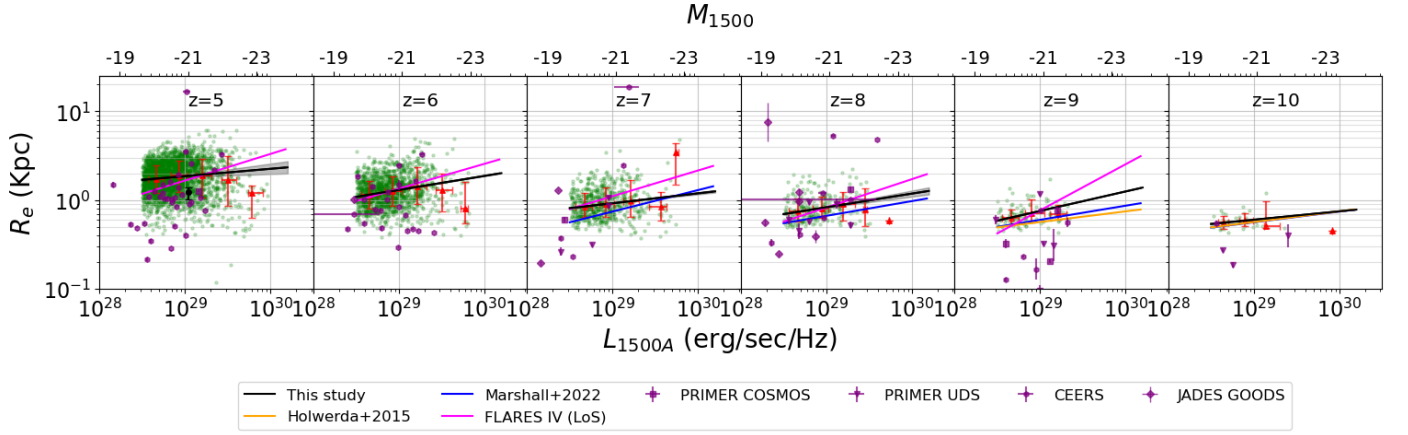


**Fig. 7.** The UV luminosity size relation at different redshifts is shown. The y-axis shows the UV 1500 Å sizes in kpc and the x-axis shows luminosity at the same wavelength. The green scatter shows our sample of galaxies analysed with radiative transfer and then simulated observations for NIRCAM. The red plots show the median luminosity and sizes in bins of 0.3dex in luminosity with 16th and 84th percentile errorbars. The black line is an linear fit to the median luminosity and sizes fit to the power law. We also compare our sample with observational studies (Holwerda et al. 2015; Bouwens et al. 2022) and simulations (Marshall et al. 2022, FLARES IV). JWST data has been taken from Morishita et al. (2024) and Ormerod et al. (2024) for the sample with  $M^*/M_\odot \geq 10^9$  from JADES (Eisenstein et al. 2023), CEERS (Holwerda et al. 2024) and PRIMER survey.

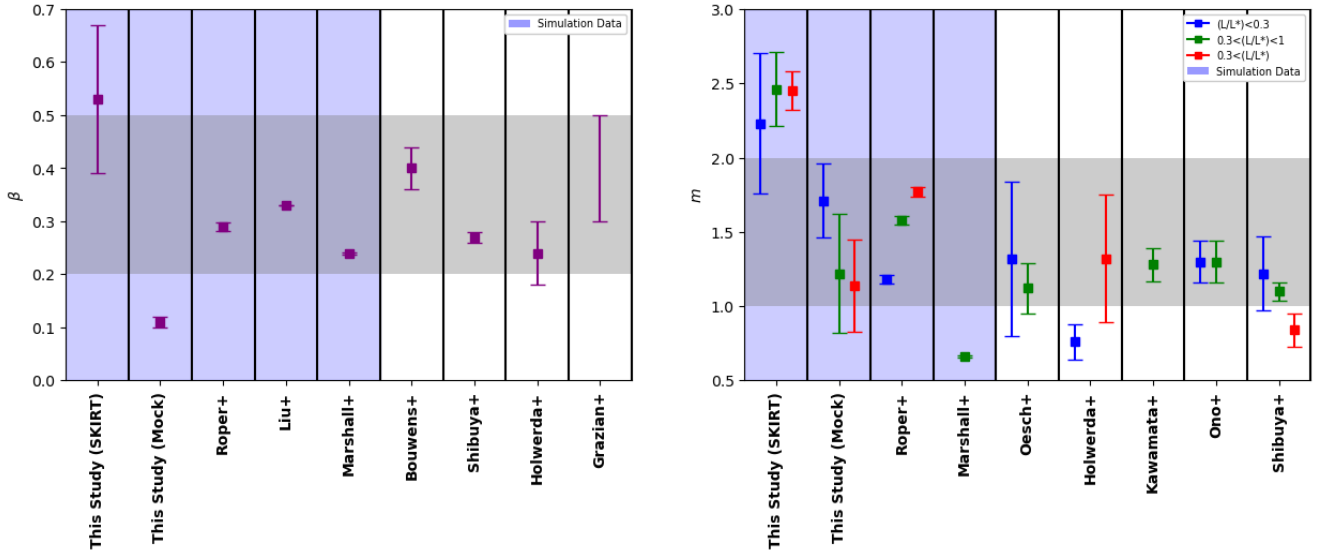


**Fig. 8. Left:** Comparison of the size-luminosity slopes ( $\beta$ ) in relation with other studies (Roper et al. 2022; Liu et al. 2017; Marshall et al. 2022; Bouwens et al. 2022; Shibuya et al. 2015; Holwerda et al. 2015; Grazian et al. 2012) at  $z=7$  (blue shaded region are simulation studies) is shown. **Right:** Comparison of the UV size evolution slopes ( $m$ ) in relation with other studies (Roper et al. 2022; Marshall et al. 2022; Oesch et al. 2010; Holwerda et al. 2015; Kawamata et al. 2018; Ono et al. 2013; Shibuya et al. 2015) is shown.

Redshift(z)	Slope of Best Fit Line			
	SNR 5	SNR 10	SNR 15	SNR 20
5	0.40	0.54	0.64	0.70
6	0.42	0.56	0.64	0.73
7	0.45	0.56	0.63	0.71
8	0.59	0.71	0.83	0.89
9	0.75	0.91	1.04	1.10
10	0.81	0.94	1.07	1.16

**Table 2.** Slopes of Best Fit Line ( $y=mx$ , no intercept) where  $y$  is mock image effective radius and  $x$  is simulation effective radius at different signal to noise ratios

vational and simulated data. We use `curve_fit` (non-linear least-squares fitting), from `SCIPY` (Virtanen et al. 2020), to produce fits and the error are generated by the covariance matrix.

Redshift	$\beta$ from SKIRT	$\beta$ from Mock Images
5	$0.6299 \pm 0.0133$	$0.0824 \pm 0.0489$
6	$0.6266 \pm 0.0275$	$0.1578 \pm 0.0027$
7	$0.5936 \pm 0.0249$	$0.1114 \pm 0.0102$
8	$0.6988 \pm 0.0815$	$0.1535 \pm 0.0289$
9	$0.4268 \pm *$	$0.2197 \pm *$
10	$0.2995 \pm *$	$0.2988 \pm *$

**Table 3.**  $\beta$  at different redshifts for radiative transfer output and the mock images (SNR=15) created.

Our analysis shows a non evolving  $\beta$  with increasing redshift (See Table 3). This agrees with Shibuya et al. (2015).<sup>4</sup> It is also worth noting that, our sample lies higher than intercepts of other studies due to a bias towards more massive objects. A comparative luminosity-size relation for various size calculation is present in Figure D.1. We see a positive  $\beta$  in agreement with major observational studies (Holwerda et al. 2015; Grazian et al. 2012; Bouwens et al. 2022). In contrast to these studies we see a non-evolving  $\beta$  (similar to Shibuya et al. (2015)). See Figure 8 for comparison with other studies at  $z=7$ .

We also plotted our luminosities and sizes in log against each other at different wavelengths to see how the effect of dust evolves as a function of wavelength (see Figure B.1). Dust causes the total luminosity to decrease and as a result size increases due to dust obscuring the bright centres of the galaxies. With increasing wavelength, the decrease in luminosity is not as significant and this makes the slope decrease. This follows well with the work in Marshall et al. (2022) and FLARES IV.

### 3.3. Size Evolution with redshift

We also explore the evolution of sizes with redshift. Since intrinsic luminosity is related to stellar mass, we bin the data in mass bins of 0.5 dex. Higher mass galaxies tend to have a higher luminosity. We then choose the mass bin of  $9.5 < M^*/M_\odot < 10$  which is commonly used in literature (Shibuya et al. 2015; Mosleh et al. 2012). This bin is also sufficiently populated in all redshifts with a good spread of luminosities. We then fit (using Equation 2) our sizes for these mass bins for three luminosity samples:

1.  $0.3 > \frac{L_{UV}}{L_{z=3}} > 0.3$
2.  $\frac{L_{UV}}{L_{z=3}} > 0.3$

<sup>4</sup> ( $z=9,10$  has only 2 sufficiently populated luminosity bins making the error margins incalculable)

3.  $1 > \frac{L_{UV}}{L_{z=3}} > 0.3$

We use `curve_fit` (non-linear least-squares fitting), from `SCIPY` (Virtanen et al. 2020), to produce the fits, and the errors are generated from the covariance matrix. For the UV luminosity bins,  $m = 1.71^{+0.25}$ ,  $1.14^{+0.31}$ ,  $1.22^{+0.40}$  respectively. Compared to the other studies, the mock image size evolution is similar to the observation studies (as seen in Figure 8), further testifying our process of mock image creation. The radiative transfer output is free of noise leading to a slightly steeper  $m$  value. See Figure 8 to see comparison with other studies. FLARES galaxies in this study match very well with observational studies. We also get consistent slope values to (Costantin et al. 2023), who analysed similar mock NIRCcam observations using TNG50 simulations at  $2\mu\text{m}$  and  $2.6\mu\text{m}$ , stating  $m = 1.26$  and  $m = 1.15$  respectively.

### 3.4. UV Size Evolution with Stellar Mass

UV size evolution against stellar mass has been analysed in simulation study using THESAN (Shen et al. 2024) and TNG50 (Costantin et al. 2023). The intrinsic sizes of galaxies show a negative correlation with increasing stellar mass ( $M^*/M_\odot \geq 10^{8.0}$ ). FLARES intrinsic sizes also show a bi-modal negative size stellar mass correlation (Roper et al. 2023). In recent CEERS survey, Ward et al. (2024) has shown a positive correlation between stellar mass and sizes. This is also consistent with pre JWST studies (Mosleh et al. 2012; Grazian et al. 2012; Ono et al. 2013). This similar relation when analysed in our study through radiative transfer and mock observations, results in positive correlation of stellar mass and size agreeing with the observations. In Figure 9 when the galaxies are binned in stellar mass, the UV sizes of galaxies show a slight increase of the slope with increasing mass, with the mock observation sizes showing a positive, but nearly flat evolution. As expected for the same stellar masses, galaxies at lower redshift are larger in size.

## 4. FIR Size Analysis

We compare the sizes in FIR regime by various methods used to study the spectrum. We also discuss the size evolution against cosmic time and its comparison with observational sizes.

### 4.1. Comparison of IR sizes by various methods

We use the ALMA images produced as described in Section 2.6.3 and calculate the sizes using the circular aperture growth curve discussed earlier. We also calculate the sizes of arbitrary photometric IR ( $50\mu\text{m}$ ) images using `STATMORPH`. Due to the effects of noise and PSF, the simulation sizes are bigger than both high-resolution ALMA and photometric sizes. Figure 10 compares the sizes in simulations and the high resolution observations methods of  $50\mu\text{m}$  photometry and ALMA mock imaging ( $\approx 0.01''$  angular resolution) and also observations like ALMA imaging ( $\approx 0.3''$  angular resolution). It shows that a high resolution photometry will be able to measure size with a higher accuracy than ALMA sizes at high resolution. For ALMA at  $\approx 0.01''$  angular resolution the low-surface brightness extended emissions of a galaxy will be lost and sensitivity while at  $\approx 0.3''$  angular resolution, small scale structures in the galaxy can be resolved. In this resolution only nearly half the galaxies are resolved.

We also compared our sizes to the recent study of Mitsuhashi et al. (2023) using similar method of observation (low angu-



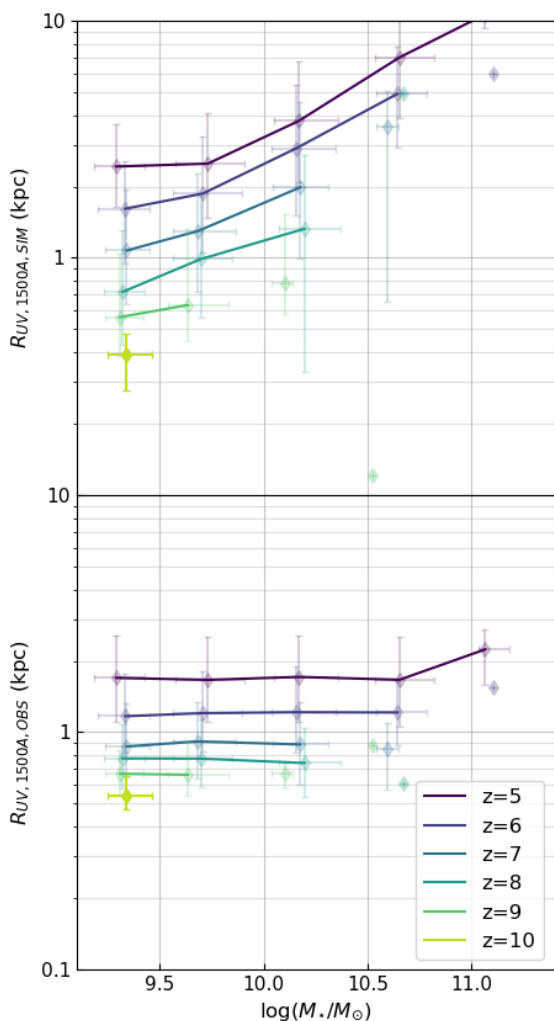


**Fig. 9.** **Upper panel:** The evolution of the UV simulation sizes (y-axis, in kpc) as function of stellar mass (x-axis) for  $z \in [5, 10]$ . **Lower panel:** Evolution of sizes from mock observations as function of stellar mass.

lar resolution,  $\approx 0.3''$ ). Figure 11 shows our  $z = 5 - 6$ , low angular resolution ( $\approx 0.3''$ ) simulated observations compared to high resolution ( $\approx 0.01''$  angular resolution) observations at  $158 \mu\text{m}$ . Ikeda et al. (2024) find that the [CII] emission sizes in CRISTAL galaxies range from 0.5-3.5 kpc with an mean of 1.9 kpc at  $z=4-6$ . For similar redshift range mock ALMA sizes for FLARES range from 0.42-3.32 kpc (99th percentile). It is important to note that nearly half of the galaxies are unresolved (2720 of 5616 or 48.43% unresolved) as also shown in the figure. The intrinsic sizes of galaxies in FLARES for the same mass and redshift range as Mitsuhashi et al. (2023); Ikeda et al. (2024) are much lower ( $\approx 10$  times) than the beam size of observations. The physical process which might be responsible for the extended nature of  $158 \mu\text{m}$  emission have been discussed in detail in Ikeda et al. (2024); Gullberg et al. (2018), but there could also be some observational effects at play. Along with the effect of beam on observations, as seen by comparing Figures 5 & F.2, at very low S/N noise close to the IR emission can act as extended emission, leading to higher sizes (See Figure G.1).

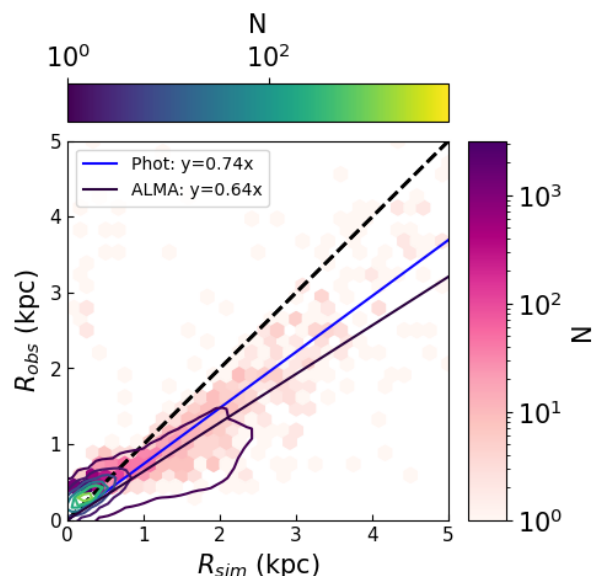


**Fig. 10.** Comparison of sizes between various IR observation methods is shown above. The plot compares IR sizes (y-axis) from mock photometry and ALMA simulations (high-resolution,  $\approx 0.01''$ ) with radiative transfer sizes (x-axis). The hex-bin plot shows the log mapped distribution of photometric sizes whereas the contours shows the log mapped distribution of mock ALMA sizes. The black line shows the 1:1 relation with the yellow line showing the best-fit  $y=mx$  relation. All ALMA sizes in this plot of high angular resolution ( $\approx 0.01''$  angular resolution)

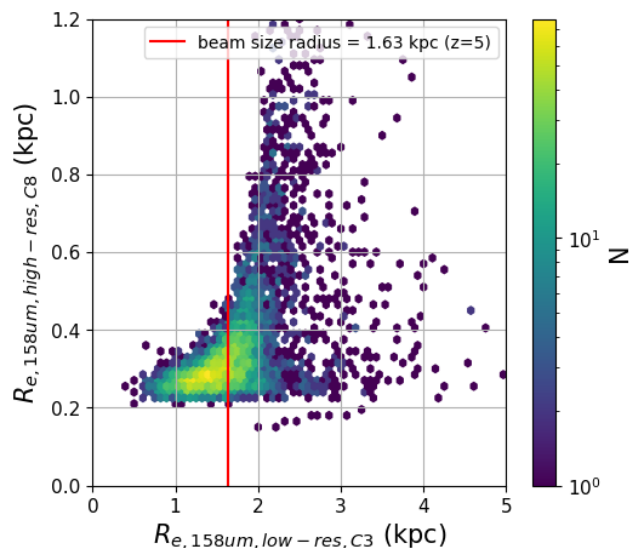


**Fig. 11.** Comparison of  $158 \mu\text{m}$  sizes between low ( $\approx 0.3''$ , C3) and high ( $\approx 0.01''$ , C8) resolution ALMA configuration setup is shown above. The high resolution ( $\approx 0.01''$ , C8) sizes is on y-axis with low resolution ( $\approx 0.3''$ , C3) sizes on x-axis. The line shows the average beam size for the low resolution observations.

#### 4.2. IR Size Evolution with redshift

We evaluated the evolution of sizes in the infrared with the same process used for UV. We calculate sizes with the growth curve method and also use Statmorph to calculate sizes from the arbitrary PSF image created. Sizes in IR also follow a power law (See Figure 12). There is negligible size evolution at IR wavelengths which leads to shallower power laws, with lower slope values of  $m=0.24$  for photometry,  $m=0.16$  for ALMA at low res-

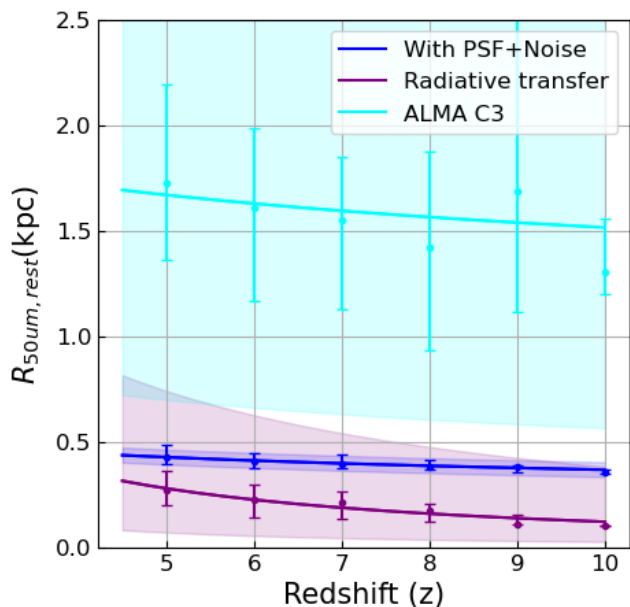


**Fig. 12.** Infrared Size Evolution with redshift at 50  $\mu\text{m}$  rest is shown with the half light radius for both the simulations and mock-photometry on the y-axis and the redshift on the x-axis. The shaded areas highlight the error margins for the fit.

olution and  $m=1.39$  for simulation size. This further alludes to most of the star formation in early universe being concentrated to compact cores, leading to less dust beyond  $r \geq 1$  kpc compared to the central core (Gullberg et al. 2019; Vijayan et al. 2024). Further physics with respect to comparison of sizes in IR against UV is discussed further in section 5.2.

#### 4.3. IR Size Evolution with Stellar Mass

We bin our galaxies in bins of 0.5 dex of Stellar Mass and see their evolution. Figure 13 shows the evolution of IR sizes with stellar mass in simulation. Besides  $z=5$  there is no significant evolution for IR sizes with increasing mass. Figures 13 also shows the IR size evolution against stellar mass for photometric observations and ALMA low/high resolution observations respectively. It is important to note that at low ALMA resolution, a lot of the sample is unresolved. The IR sizes of galaxies show no significant evolution with increasing stellar mass. And similar to UV, for same stellar mass, galaxies at lower redshift are larger in size.

## 5. Panchromatic Analysis

### 5.1. Size Evolution with wavelengths

To evaluate the size evolution with wavelength we first normalise the evolution by dividing the sizes by 1500  $\text{\AA}$  and 500  $\mu\text{m}$  sizes in IR (All sizes are sizes from simulations). Figure 14 shows the evolution of median sizes at UV wavelengths. These sizes are normalized with the sizes at 1500  $\text{\AA}$ . For each redshift we observe a huge decrease (0.4 times at 0.4  $\mu\text{m}$ ) in size with increasing wavelength. The size reduction is likely due to increasing effect of dust attenuation with increasing wavelengths. This follows well with effect of dust shown in Marshall et al. (2022) and FLARES IV, as well as our analysis in Appendix B.

Figure 14 also shows the evolution of median sizes in FIR against wavelength. These sizes are normalized with the sizes at

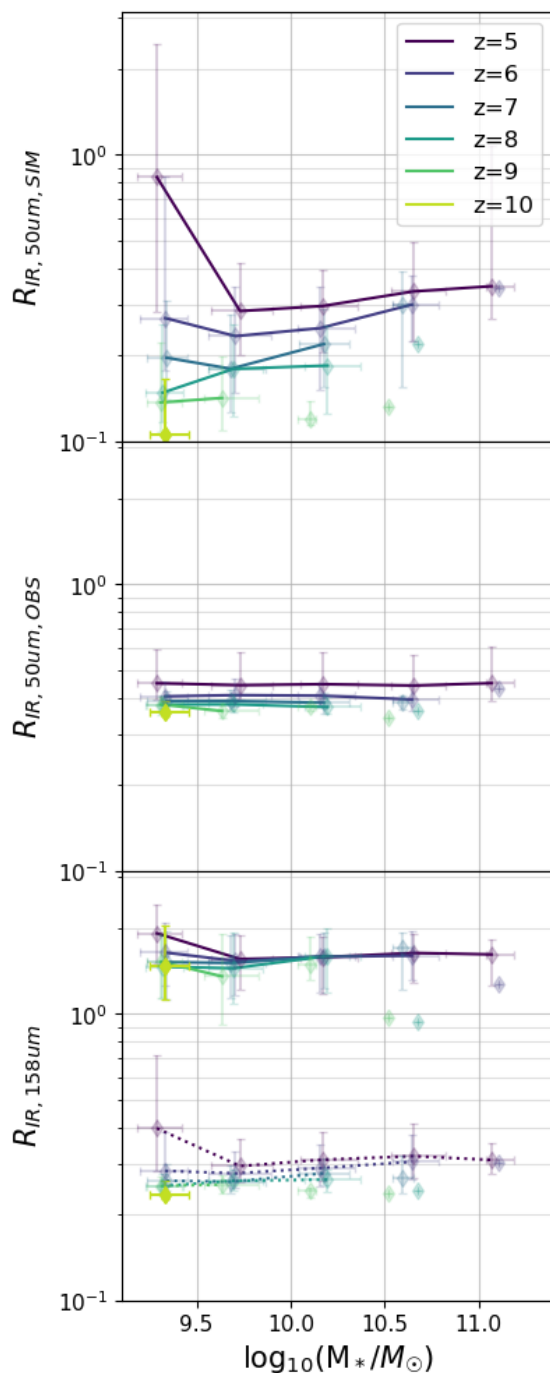


**Fig. 13.** Upper panel: The median sizes(y-axis) of 50 $\mu\text{m}$  in simulations as a function of stellar mass(x-axis). Middle panel: The evolution of mock photometric observational sizes. Lower panel: shows the evolution of ALMA observed sizes. in the lower panel the sizes are represented by the dotted lines and the low angular resolution ( $\approx 0.3''$ ) sizes are represented by the solid lines.

500  $\mu\text{m}$ . For the FIR, which is not as effected by dust, we see slight positive trend in sizes with increasing wavelengths, due to the prevalence of hotter dust (probed by shorter wavelengths) in the centres. Popping et al. (2022) showed a similar constant sizes with increasing wavelength in the observed frame.



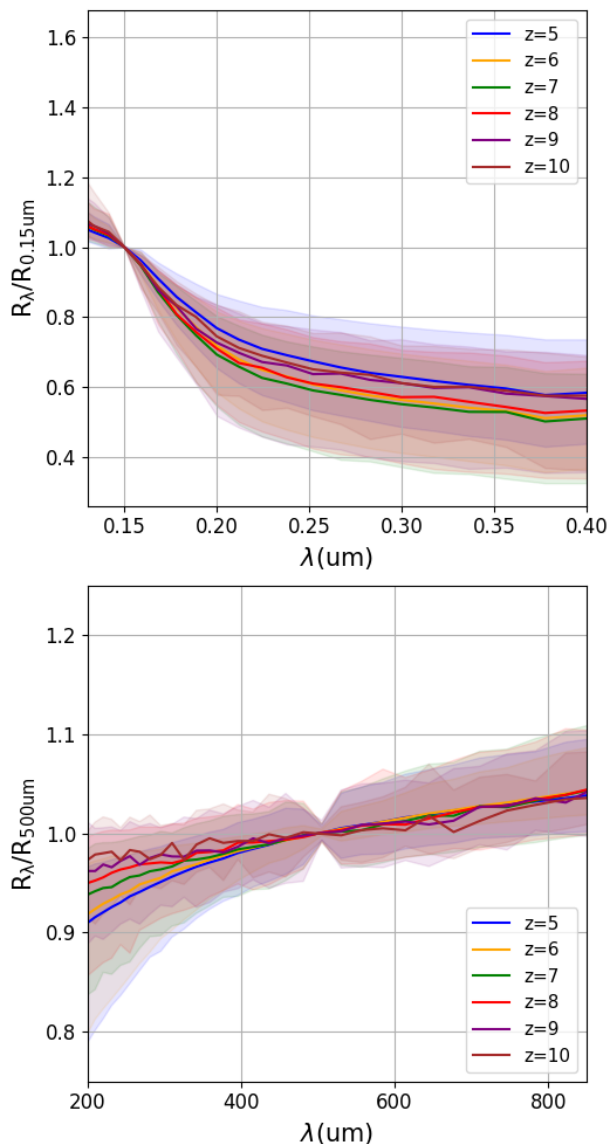


**Fig. 14.** Evolution of normalized size with wavelength is shown in UV (upper panel) and IR (lower panel). The solid curves correspond to the median of the distribution, whereas the color-shaded regions mark the one-sigma scatter of the distribution

## 5.2. Comparison of Sizes in UV and IR

UV emission is pre-dominantly from young stars within galaxies, hence size evolution in UV spectrum is indicative of the progression of unobscured star formation in galaxies. IR emission helps us to understand the distribution of dust, and unlike the UV sizes, IR sizes do not evolve significantly either over time or with increasing stellar mass (See Section 3.4 and 4.3). This is consistent with studies like Popping et al. (2022). The increasing ratio of UV/IR size with increasing mass as seen in Figure 15 is driven by inside-out growth of star formation, rather than an increase in the dust obscuration within the centres. To analyse this size evolution ratio in UV and IR, we also look at previous FLARES work to understand the evolution of star formation and the processes behind it.

Roper et al. (2023) details the different physical mechanisms driving the formation and evolution of compact galaxies. The

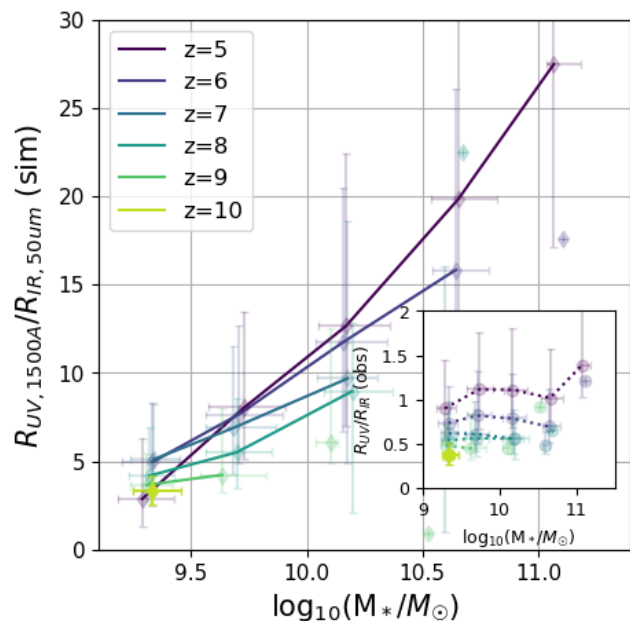


**Fig. 15.** Ratio of sizes from simulations with no observational effects (main figure) as well mock observations (inset figure) at 1500 Å with observations like ALMA configuration is shown for UV and IR spectrum in stellar mass bins of 0.5 dex, with median values plotted as data-points. The error-bars denote the 16th and 84th percentile values. Only sufficiently populated bins ( $N > 20$ ) have been used to plot the lines.

study presents physics behind star formation in the early universe compact galaxies. As cold and very dense gases are required for star formation, the star formation criteria in the FLARE (or EAGLE) simulation, imposes a critical gas density, which is inversely related to the gas phase metallicity. The cores of early galaxies are enriched by metals leading to dense star-forming as well as dust attenuated cores. When at later times the outer regions get enriched with metals, inside out growth starts taking place, also leading to bigger UV sizes. More details of these processes can be found in the referred study.

Roper et al. (2023) finds that massive compact galaxies can form following two different evolution paths. It shows that galaxies at  $z = 5$  can have progenitors which formed at  $z > 10$  in pristine environments with low metal enrichment. Stars in such progenitors are formed at high densities, and these galaxies remain compact throughout their evolution. This is the compact formation path. The other path as shown by Roper et al. (2023) shows that galaxies can also transition from being diffused to compact and these galaxies have partially metal enriched progenitors (at  $z < 10$ ). These galaxies become compact at lower redshifts ( $z < 6$ ) due to runaway star formation in their cores. Amongst the galaxies, low stellar mass galaxies ( $M^* \leq 10^{8.8} M_\odot$ ) are diffused clumpy systems that do not undergo a transition in size. Galaxies with stellar mass in range of  $10^{8.8} M_\odot \leq M^* \leq 10^{9.8} M_\odot$  show a significant decrease in size due to efficient localised cooling of gas. Figure 15 shows the UV/IR size ratio as a function of redshift for both radiative transfer sizes with no observational effects as well as mock observations for JWST and ALMA. We can see that for intrinsic radiative sizes for the stellar masses in range  $10^{9.0} M_\odot \leq M^* \leq 10^{10.0} M_\odot$ , the ratio decreases at lower  $z$  corresponding to the mass range of transition between diffused and compact galaxies presented in Roper et al. (2023). But when the mock observations for ALMA (low angular resolution similar to Mitsuhashi et al. (2023),  $\approx 0.3''$ ) and JWST are used, the

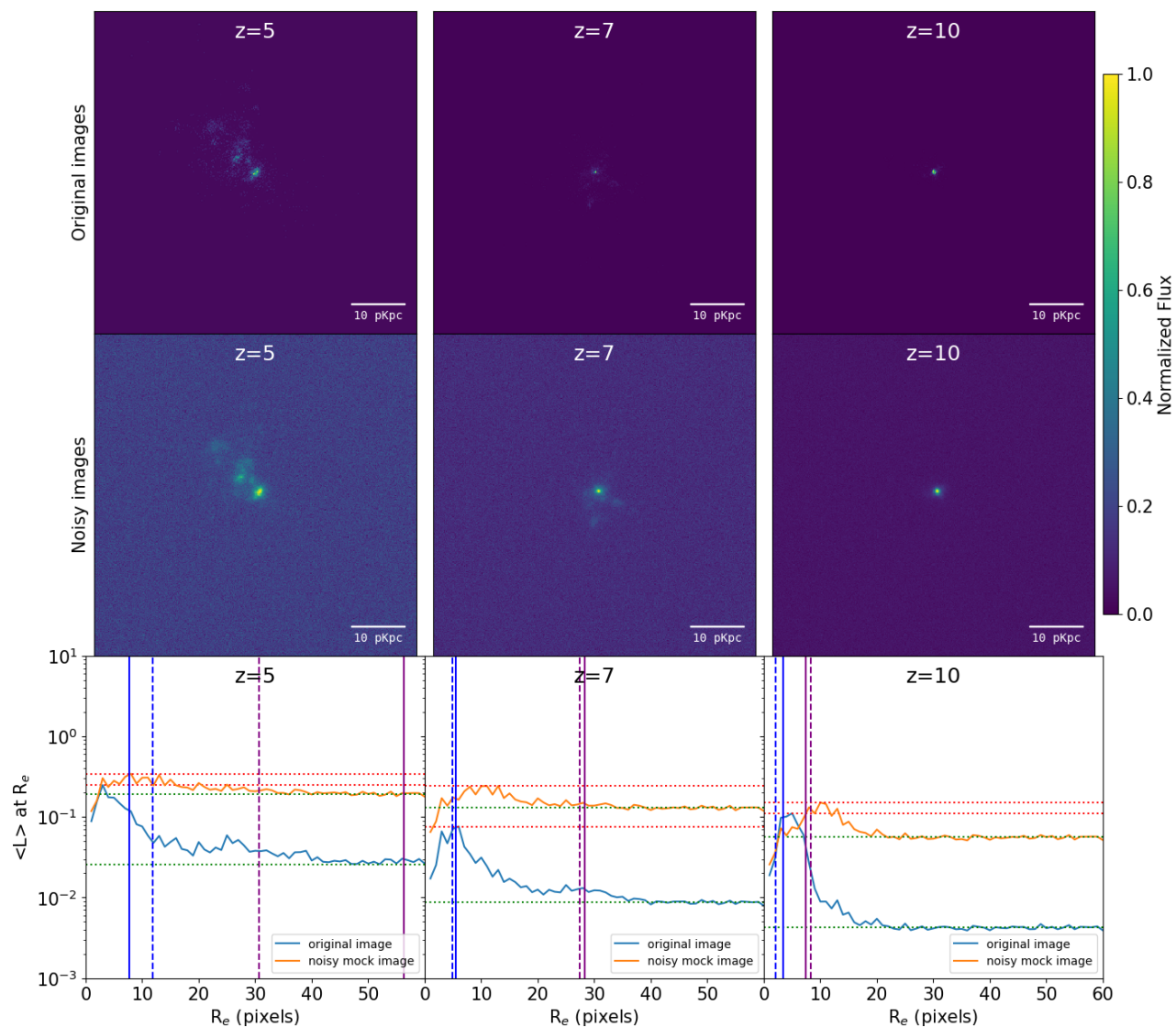


**Fig. 16.** Brightness comparison between original and noisy image is shown for a sample redshift 5, 7 & 10 galaxies with size offset at SNR=5. The bottom row shows the mean luminosity of pixels at each radius (y-axis) calculated by finding pixel luminosities at the edge of the aperture and dividing it by circumference) plotted against the radius (x-axis) for the normalized images. The center for these luminosities is assumed as the centre of potential as defined in the simulations. The red lines indicate the maximum brightness and the green line shows the median brightness. The blue solid and dashed lines show the  $r_{20}$  of original and noisy image respectively. The purple solid and dashed lines show the  $r_{80}$  of original and noisy images respectively. Panel for  $z=5$  shows the case of underestimation,  $z=7$  of near parity and  $z=10$  shows overestimation.

ratio are significantly lower and IR sizes can be predicted to be larger than UV sizes as well as shown by Pozzi et al. (2024); Fudamoto et al. (2022); Mitsuhashi et al. (2023). Similar curves for mock observation ratios with high angular resolution with ALMA, mimic the size ratio curved from simulations very well.

A further spatial analysis between UV and IR will be presented in a study in preparation (Punyasheel et al. in prep).

## 6. Effect of Noise and PSF

PSF describes the spread of the flux over a range of pixels for a point source due to the diffraction of light entering the optics of an observatory. The optics spreads the sources in a pattern around its surroundings, making the surrounding regions of bright sources even brighter. Along with this, Gaussian noise has increases or decreases the brightness of a pixel. Compared to the brightest pixel, the relative brightness of very faint/median pixels

can change significantly. Since we calculate half light radius by measuring total luminosity inside a certain aperture and comparing it with the total luminosity (hence dealing in relative brightness), this jumping of pixels to different brightness bins affects the observed sizes.

We took a sample of images from different redshifts and normalized them and then calculated average brightness of a pixel at different radii (radii are calculated from the center of potential defined in the simulations to perform consistent analysis across all galaxies). Figure 16 compares the original radiative transfer output to the noisy image. We measure and compare the shift in relative luminosity profiles of the original and final noisy images to see the effect of relative effect of noise with increasing redshift. The higher the redshift, the more the median brightness pixels are closer in magnitude to the maximum brightest pixels. It is also apparent that the total luminosity of a galaxy will be lost due to noise reduction while applying a minimum thresh-



Relative Brightness	z					
	5	6	7	8	9	10
(0.0,0.2]	96.49	95.33	93.81	91.23	87.63	85.45
(0.2,0.4]	2.60	2.87	3.53	4.43	5.59	76.24
(0.4,0.6]	0.66	1.16	1.58	2.33	3.64	4.14
(0.6,0.8]	0.18	0.46	0.71	1.31	1.78	2.17
(0.8,1.0]	0.06	0.18	0.36	0.70	1.35	2.00

**Table 4.** Mean percentage of Pixels is shown in each relative brightness bins after normalizing the images in radiative transfer output in a square aperture of width equal to  $4R_e$  ( $R_e$  is intrinsic RT size).

Relative Brightness	z					
	5	6	7	8	9	10
(0.0,0.2]	0.40	0.41	0.19	0.25	0.13	0.06
(0.2,0.4]	29.18	25.85	18.64	22.56	12.48	10.02
(0.4,0.6]	59.28	61.23	61.95	56.70	48.37	44.97
(0.6,0.8]	10.02	10.93	15.76	15.74	28.82	35.99
(0.8,1.0]	1.11	1.58	3.47	4.76	10.21	8.96

**Table 5.** Mean percentage of Pixels is shown in each relative brightness bins after normalizing the images in mock noisy images (SNR=5) in a square aperture of width equal to  $4R_e$  ( $R_e$  is intrinsic RT size).

old pixel value as also elaborated in Varadaraj et al. (2024). This leads to fewer pixels being evaluated for non-parametric size calculation. We show the mean percentage of pixels for galaxies in each redshift from our sample in bins of relative brightness for radiative transfer output and mock noisy images in Tables 4 and 5 respectively. This impact of noise is dependent on observational parameters and filters used, affecting the depth of observations. Varadaraj et al. (2024) finds that low wavelengths filters (F115W) find a larger impact of noise on sizes than higher wavelength filters (F444W). Noise washes out faint sources effectively at low depth leading to higher offset between clean mock galaxy sizes and the observed sizes than at higher depths.

Using combined observational effects of noise, pixel scale and PSF our study at lower redshifts shows that galaxy centers are not extremely bright relative to the median luminosity regions, and hence Gaussian noise is able to move many pixels to a higher luminosity. Due to the effect of PSF, noisy images also have brighter centers, while the low luminous parts of a galaxy blend with noise. The loss of luminosity to noise triumphs the effect of PSF at lower SNR resulting in a increment of the  $r_{20}$  (radius at which 20 percent light is present) and a reduction of  $r_{80}$  (radius at which 80 percent light is present). This leads to high underestimation of the galaxy sizes at lower redshifts. With increasing redshift the galaxy centers are becoming comparatively brighter which is further strengthened by PSF. This leads to underestimation of sizes with higher factors compared to lower redshifts. With increasing SNR, lesser and lesser low luminous parts of the galaxy blend into the noise, decreasing the observed luminosity. This leads to  $r_{20}$  decreasing due to the center. The opposite effect is seen with  $r_{80}$  and  $r_{50}$  which increase to compensate for the lost luminosity. Hence the sizes of galaxies are being overestimated at high redshift and high SNR.

## 7. Summary and Conclusions

In this study, we perform radiative transfer using SKIRT (Camps & Baes 2015, 2020) for galaxies from the FLARE simulations to study size evolution in the UV and the far-IR at the Epoch of Reionisation ( $z \in [5, 10]$ ). This is an alternative approach to the

Line of Sight method used by many simulation studies including previous FLARES work (Roper et al. 2022; Marshall et al. 2022). Radiative transfer using Monte Carlo simulation precisely estimates the effect of dust absorption and scattering of radiation to provide a more accurate Spectral Energy Distribution. We use the results of the radiative transfer simulations to mock observations of these galaxies, for NIRCcam at rest frame FUV, to find and analyse the offset in observational sizes to actual sizes of galaxies. We also simulate imaging in the far-IR at wavelengths of  $50 \mu\text{m}$  and  $250 \mu\text{m}$  as well as interferometric observations by ALMA for  $158 \mu\text{m}$ . The images are produced by taking into account the noise as well as the PSF (for mock imaging) or beam sizes (for ALMA configuration in CASA). We analysed our galaxies for various SNRs (5,10,15 and 20). To evaluate the sizes of galaxies in the simulation, after radiative transfer, we used a curve of growth method, by using circular apertures of increasing radius from the most bound particle and interpolating the radius at which 50 percent of the light was present. To evaluate the sizes from mock photometric observations we used STATMORPH (Rodriguez-Gomez et al. 2019). Using both these methods we are able to compare the sizes of mock observations with actual sizes.

Using the above described methods, we also calculate the sizes in IR regime.

We compare the slope parameter in the power laws (Equations 1 & 2) of size evolution with cosmic time as well as size evolution against luminosity at fixed redshift, for both simulations and observations. We also analyse how the sizes vary with increasing mass and wavelengths of observations in both UV and IR. Our main findings from these studies are as follows:

1. Mock NIRCcam observations of FLARES galaxies at rest frame FUV ( $1500 \text{ \AA}$ ) show a decreasing size evolution with redshift, which is consistent with many observational studies (e.g. Oesch et al. 2010; Ono et al. 2013; Shibuya et al. 2015). These findings also closely match with the slope predictions from simulation results from Roper et al. (2022).
2. For fixed redshifts, the size-luminosity evolution of the mock observations agree with Shibuya et al. (2015); Holwerda et al. (2015); Grazian et al. (2012); Bouwens et al. (2022) study showing a positive  $\beta$ . We also find a broadly non-evolving  $\beta$  with increasing redshift similar to Shibuya et al. (2015). The  $\beta$  for mock imaging is comparatively lower than observational studies as well as simulation studies.
3. The sizes taken directly from the radiative transfer results follow a higher  $\beta$  of 0.59 at  $z=7$ . For sizes from simulation using radiative transfer, the slopes of size evolution are significantly higher than observations in all luminosity bins evaluated. This variance of slopes is due to the offset of size in observations against the inherent radiative transfer sizes.
4. Due to observational effects of noise and PSF, at lower SNR, the mock observational sizes are underestimated. While at higher SNR due to the reduced effect of noise sizes are underestimated at lower redshift ( $z = 5, 6, 7, 8$ ) in NIRCcam observations and at higher redshifts ( $z = 9, 10$ ) the sizes tend to be slightly overestimated where the effect of PSF leads to bright cores becoming bigger. The ratio of mock observation sizes to sizes in simulation is also a function of signal to noise ratio. For higher signal to noise ratios, the underestimation decreases, and overestimation creeps in for high redshift. This effect is also prominent in IR observations as both high resolution ALMA ( $\approx 0.01''$ , C3) and mock photometric  $50 \mu\text{m}$  imaging show similar variation for simulation sizes.

5. The effect of noise in low-resolution ALMA observations ( $\approx 0.3''$ ) is opposite to what is observed in UV. Noise around the signal at low SNRs appears as extended emissions, hence leading to an increase in size. The lower the observed SNR, higher the observed to intrinsic size ratio can be.
6. The sizes in IR spectrum follow the same power law as UV but the sizes are substantially smaller for very high resolution imaging. Due to less evolution in size power laws are less steep making the slope of evolution lesser to a value of 0.24 for photometric observations, 0.16 for ALMA observations and 1.39 for simulation size. The ratio of sizes in UV and IR increases with increasing mass, which is due to higher mass galaxies having higher star formation rates and being dominated by young blue stars. Low mass galaxies ( $\log_{10}(M^*/M_{\odot}) \approx 8.8-9.8$ ) at  $z < 6$  show a sudden dip in UV-IR size ratio due to transition from dispersed to compact star formation as described in Roper et al. (2023).

The variation of observed from intrinsic sizes highlights the importance of accounting for observational effects such as noise, PSF, and SNR when interpreting galaxy size measurements. As higher resolution photometry of galaxies in the EoR become increasingly available with *JWST*, the constraints on the size evolution slopes will become increasingly robust in the UV. Observational effects such as SNR and angular resolution also affect the observed ALMA sizes. Studying sizes in IR to a high accuracy will also require very high resolution observations which can resolve both small scale structures and low surface brightness extended emissions. Combining multi-wavelength studies of galaxy sizes in IR and UV can help us unravel the physics beneath dust-obscured star formation to understand the interplay of star formation, chemical enrichment and feedback.

A proper comparison between observations and theory becomes paramount to, validate, and refine our understanding of galaxy evolution. Next generation simulations must aim to not only reproduce the UV luminosity functions, but also predict the observed size and luminosity distribution of galaxies across different observed wavelengths. In the future, with instruments like Square Kilometre Array (SKA), Extremely Large Telescope (ELT) and Very Large Array (VLA) coming online, will enable us to study galaxies with unprecedented resolution and sensitivity across a wide range of wavelengths.

Coupling these next-generation multi-wavelength observations with simulations will refine our knowledge of galaxy formation and evolution at the Epoch of Re-ionisation, providing us with deeper insights into the complex interplay of gas, dust and radiation.

*Acknowledgements.* This work has been performed using the Danish National Life Science Supercomputing Center, Computerome. This work also used the DiRAC@Durham facility managed by the Institute for Computational Cosmology on behalf of the STFC DiRAC HPC Facility ([www.dirac.ac.uk](http://www.dirac.ac.uk)). The equipment was funded by BEIS capital funding via STFC capital grants ST/K00042X/1, ST/P002293/1, ST/R002371/1 and ST/S002502/1, Durham University and STFC operations grant ST/R000832/1. DiRAC is part of the National e-Infrastructure. The Cosmic Dawn Center (DAWN) is funded by the Danish National Research Foundation under grant DNRF140. We also wish to acknowledge the following open source software packages used in the analysis: NUMPY (Harris et al. 2020), SCIPY (Virtanen et al. 2020), PANDAS (pandas development team 2020), ASTROPY (Astropy Collaboration et al. 2013, 2018, 2022), PILLOW (Clark 2015), MATPLOTLIB (Hunter 2007) and STATMORPH (Rodriguez-Gomez et al. 2019). PP would also like to thank Dr. Anurag Nishad and Dr. Anumpama Sharma for guidance towards completion of his thesis leading to this study.

## References

- Astropy Collaboration, Price-Whelan, A. M., Lim, P. L., et al. 2022, *ApJ*, **935**, 167
- Astropy Collaboration, Price-Whelan, A. M., Sipőcz, B. M., et al. 2018, *AJ*, **156**, 123
- Astropy Collaboration, Robitaille, T. P., Tollerud, E. J., et al. 2013, *A&A*, **558**, A33
- Bouwens, R. J., Illingworth, G. D., Blakeslee, J. P., Broadhurst, T. J., & Franx, M. 2004, *ApJ*, **611**, L1
- Bouwens, R. J., Illingworth, G. D., van Dokkum, P. G., et al. 2022, *ApJ*, **927**, 81
- Bowler, R. A. A., Cullen, F., McLure, R. J., Dunlop, J. S., & Avison, A. 2022, *MNRAS*, **510**, 5088
- Bowler, R. A. A., Dunlop, J. S., McLure, R. J., & McLeod, D. J. 2017, *MNRAS*, **466**, 3612
- Bradley, L., Sipőcz, B., Robitaille, T., et al. 2023, *astropy/photutils*: 1.8.0
- Camps, P. & Baes, M. 2015, *Astronomy and Computing*, **9**, 20
- Camps, P. & Baes, M. 2020, *Astronomy and Computing*, **31**, 100381
- CASA Team, Bean, B., Bhatnagar, S., et al. 2022, *PASP*, **134**, 114501
- Chiang, Y.-K., Overzier, R., & Gebhardt, K. 2013, *ApJ*, **779**, 127
- Clark, A. 2015, Pillow (PIL Fork) Documentation
- Conroy, C. & Gunn, J. E. 2010, *ApJ*, **712**, 833
- Conselice, C. J. 2014, *ARA&A*, **52**, 291
- Costantin, L., Pérez-González, P. G., Vega-Ferrero, J., et al. 2023, *ApJ*, **946**, 71
- Crain, R. A., Schaye, J., Bower, R. G., et al. 2015, *MNRAS*, **450**, 1937
- Davé, R., Anglés-Alcázar, D., Narayanan, D., et al. 2019, *MNRAS*, **486**, 2827
- Davis, M., Efstathiou, G., Frenk, C. S., & White, S. D. M. 1985, *ApJ*, **292**, 371
- Dolag, K., Borgani, S., Murante, G., & Springel, V. 2009, *MNRAS*, **399**, 497
- Eisenstein, D. J., Willott, C., Alberts, S., et al. 2023, *arXiv e-prints*, [arXiv:2306.02465](https://arxiv.org/abs/2306.02465)
- Feng, Y., Di-Matteo, T., Croft, R. A., et al. 2016, *MNRAS*, **455**, 2778
- Ferguson, H. C., Dickinson, M., Giavalisco, M., et al. 2004, *ApJ*, **600**, L107
- Ferreira, L., Conselice, C. J., Sazonova, E., et al. 2023, *ApJ*, **955**, 94
- Franx, M., van Dokkum, P. G., Förster Schreiber, N. M., et al. 2008, *ApJ*, **688**, 770
- Fudamoto, Y., Smit, R., Bowler, R. A. A., et al. 2022, *ApJ*, **934**, 144
- Grazian, A., Castellano, M., Fontana, A., et al. 2012, *A&A*, **547**, A51
- Groves, B., Dopita, M. A., Sutherland, R. S., et al. 2008, *ApJS*, **176**, 438
- Gullberg, B., Smail, I., Swinbank, A. M., et al. 2019, *MNRAS*, **490**, 4956
- Gullberg, B., Swinbank, A. M., Smail, I., et al. 2018, *ApJ*, **859**, 12
- Harris, C. R., Millman, K. J., van der Walt, S. J., et al. 2020, *Nature*, **585**, 357–362
- Högbom, J. A. 1974, *A&AS*, **15**, 417
- Holwerda, B. W., Bouwens, R., Oesch, P., et al. 2015, *ApJ*, **808**, 6
- Holwerda, B. W., Hsu, C.-C., Hathi, N., et al. 2024, *MNRAS*, **529**, 1067
- Huang, K.-H., Ferguson, H. C., Ravindranath, S., & Su, J. 2013, *ApJ*, **765**, 68
- Hunter, J. D. 2007, *Computing in Science and Engineering*, **9**, 90
- Ikeda, R., Tadaki, K.-i., Mitsuhashi, I., et al. 2024, *arXiv e-prints*, [arXiv:2408.03374](https://arxiv.org/abs/2408.03374)
- Jiang, L., Egami, E., Fan, X., et al. 2013, *ApJ*, **773**, 153
- Kawamata, R., Ishigaki, M., Shimasaku, K., Oguri, M., & Ouchi, M. 2015, *ApJ*, **804**, 103
- Kawamata, R., Ishigaki, M., Shimasaku, K., et al. 2018, *ApJ*, **855**, 4
- Li, A. 2008, *arXiv e-prints*, [arXiv:0808.4123](https://arxiv.org/abs/0808.4123)
- Li, Q., Narayanan, D., & Davé, R. 2019, *MNRAS*, **490**, 1425
- Liu, C., Mutch, S. J., Poole, G. B., et al. 2017, *MNRAS*, **465**, 3134
- Lovell, C. C., Thomas, P. A., & Wilkins, S. M. 2018, *MNRAS*, **474**, 4612
- Lovell, C. C., Vijayan, A. P., Thomas, P. A., et al. 2021, *MNRAS*, **500**, 2127
- Magnelli, B., Boogaard, L., Decarli, R., et al. 2020, *ApJ*, **892**, 66
- Marshall, M. A., Mutch, S. J., Qin, Y., Poole, G. B., & Wyithe, J. S. B. 2019, *MNRAS*, **488**, 1941
- Marshall, M. A., Wilkins, S., Di Matteo, T., et al. 2022, *MNRAS*, **511**, 5475
- Mitsuhashi, I., Tadaki, K.-i., Ikeda, R., et al. 2023, *arXiv e-prints*, [arXiv:2311.17671](https://arxiv.org/abs/2311.17671)
- Mo, H. J., Mao, S., & White, S. D. M. 1998, *MNRAS*, **295**, 319
- Morishita, T., Stiavelli, M., Chary, R.-R., et al. 2024, *ApJ*, **963**, 9
- Mosleh, M., Williams, R. J., Franx, M., et al. 2012, *ApJ*, **756**, L12
- Nelson, D., Pillepich, A., Springel, V., et al. 2019, *MNRAS*, **490**, 3234
- Oesch, P. A., Bouwens, R. J., Carollo, C. M., et al. 2010, *ApJ*, **709**, L21
- Ono, Y., Ouchi, M., Curtis-Lake, E., et al. 2013, *ApJ*, **777**, 155
- Ormerod, K., Conselice, C. J., Adams, N. J., et al. 2024, *MNRAS*, **527**, 6110
- pandas development team, T. 2020, *pandas-dev/pandas*: Pandas
- Perrin, M. D., Sivaramakrishnan, A., Lajoie, C.-P., et al. 2014, in Society of Photo-Optical Instrumentation Engineers (SPIE) Conference Series, Vol. 9143, *Space Telescopes and Instrumentation 2014: Optical, Infrared, and Millimeter Wave*, ed. J. Oschmann, Jacobus M., M. Clampin, G. G. Fazio, & H. A. MacEwen, **91433X**



- Perrin, M. D., Soummer, R., Elliott, E. M., Lallo, M. D., & Sivaramakrishnan, A. 2012, in *Society of Photo-Optical Instrumentation Engineers (SPIE) Conference Series*, Vol. 8442, *Space Telescopes and Instrumentation 2012: Optical, Infrared, and Millimeter Wave*, ed. M. C. Clampin, G. G. Fazio, H. A. MacEwen, & J. Oschmann, Jacobus M., 84423D
- Pillepich, A., Nelson, D., Springel, V., et al. 2019, *MNRAS*, 490, 3196
- Popping, G., Pillepich, A., Calistro Rivera, G., et al. 2022, *MNRAS*, 510, 3321
- Pozzi, F., Calura, F., D'Amato, Q., et al. 2024, *A&A*, 686, A187
- Pozzi, F., Calura, F., Fudamoto, Y., et al. 2021, *A&A*, 653, A84
- Rodriguez-Gomez, V., Snyder, G. F., Lotz, J. M., et al. 2019, *MNRAS*, 483, 4140
- Roper, W. J., Lovell, C. C., Vijayan, A. P., et al. 2023, *MNRAS*, 526, 6128
- Roper, W. J., Lovell, C. C., Vijayan, A. P., et al. 2022, *MNRAS*, 514, 1921
- Schaye, J., Crain, R. A., Bower, R. G., et al. 2015, *MNRAS*, 446, 521
- Sérsic, J. L. 1963, *Boletín de la Asociación Argentina de Astronomía La Plata Argentina*, 6, 41
- Shen, X., Vogelsberger, M., Borrow, J., et al. 2024, *arXiv e-prints*, arXiv:2402.08717
- Shibuya, T., Ouchi, M., & Harikane, Y. 2015, *ApJS*, 219, 15
- Springel, V., White, S. D. M., Jenkins, A., et al. 2005, *Nature*, 435, 629
- Springel, V., White, S. D. M., Tormen, G., & Kauffmann, G. 2001, *MNRAS*, 328, 726
- Stanway, E. R. & Eldridge, J. J. 2018, *MNRAS*, 479, 75
- Steidel, C. C., Adelberger, K. L., Giavalisco, M., Dickinson, M., & Pettini, M. 1999, *ApJ*, 519, 1
- Steinacker, J., Baes, M., & Gordon, K. D. 2013, *ARA&A*, 51, 63
- Stetson, P. B. 1990, *PASP*, 102, 932
- Varadaraj, R. G., Bowler, R. A. A., Jarvis, M. J., et al. 2024, *arXiv e-prints*, arXiv:2401.15971
- Vijayan, A. P., Clay, S. J., Thomas, P. A., et al. 2019, *MNRAS*, 489, 4072
- Vijayan, A. P., Lovell, C. C., Wilkins, S. M., et al. 2021, *MNRAS*, 501, 3289
- Vijayan, A. P., Thomas, P. A., Lovell, C. C., et al. 2024, *MNRAS*, 527, 7337
- Vijayan, A. P., Wilkins, S. M., Lovell, C. C., et al. 2022, *MNRAS*, 511, 4999
- Virtanen, P., Gommers, R., Oliphant, T. E., et al. 2020, *Nature Methods*, 17, 261
- Ward, E., de la Vega, A., Mobasher, B., et al. 2024, *ApJ*, 962, 176
- Weingartner, J. C. & Draine, B. T. 2001, *ApJ*, 548, 296
- Wu, X., Davé, R., Tacchella, S., & Lotz, J. 2020, *MNRAS*, 494, 5636
- Xie, Y., Li, A., & Hao, L. 2017, *ApJS*, 228, 6
- Yates, R. M., Hendriks, D., Vijayan, A. P., et al. 2024, *MNRAS*, 527, 6292

## Appendix A: NIRCam Calculated Resolutions

The resolution used for NIRCam based on filters and redshift, calculated by (Astropy Collaboration et al. 2013, 2018, 2022) is presented in Table A.1.

Redshift(z)	Resolution(pxs by pxs)
5	302x302
6	332x332
7	363x363
8	393x393
9	425x425
10	456x456

**Table A.1.** NIRCam Image Resolution at different redshifts for a field of view of 60 pkpcx60 pkpc(size of radiative transfer simulations)

The radiative transfer outputs are regridded to these resolutions for mocking observations.

## Appendix B: Effect of Dust on Luminosity

The effect of dust decreases with increasing wavelength. In Figure B.1 we plotted the slopes of sizes against luminosities for all the wavelengths that we probed.

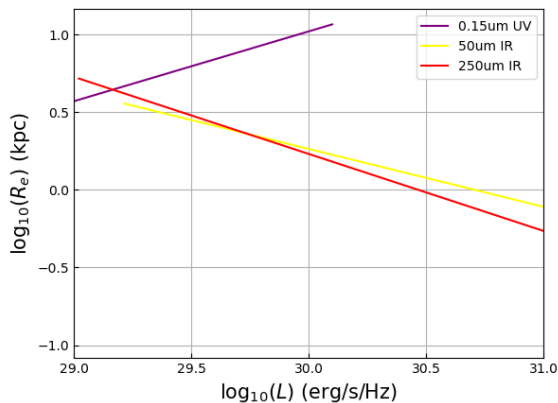


**Fig. B.1.** Effect of dust on Luminosity is seen for increasing wavelength ( $z=5$ ) by plotting the best fit line of sizes on the y-axis and the luminosity on the x-axis for various wavelengths. The slopes are seen to decrease with the increase in wavelength.

## Appendix C: Size-Offset Relation to Galaxy Characteristics

To determine why there is an offset between observational sizes and simulational sizes, in Figure C.1, we plot the ratio of sizes in simulations to observational size on a plane of FUV luminosity and stellar mass, seeing no significant correlation.

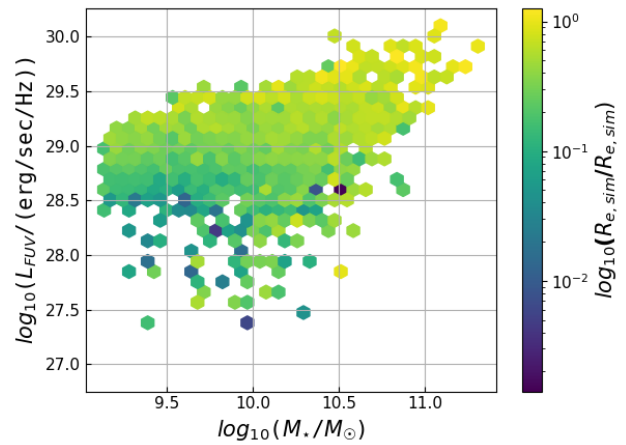


**Fig. C.1.** Ratio of simulation to observational sizes is plotted in the plane of stellar mass (x-axis) and FUV luminosity (y-axis) for galaxies at  $z=5$

## Appendix D: Size-luminosity Relation Comparison

To show the effect of using a non parametric pixel based method as presented in FLARES IV to this studies' curves of growth method we fit the size luminosity relation for both size calculation methods to the radiative transfer output in Figure D.1.

## Appendix E: Simulated observations in a singular noise field

We analysed the galaxies when they are placed in a singular noise field to analyse the effect of same observation time on detection and non detection. We found that out of a total sample of 6890 galaxies 167 will not be detected at 1500 Å by JWST. The galaxies which are not detected have low luminosities compared to the galaxies which were detected for similar stellar mass (See Figure E.1). On further visual inspection of the galaxy images, we see that these galaxies are very dispersed and hence at lower SNR, a lot of the detail in these galaxies falls below the noise depth. These galaxies also have a comparatively lower SFR (See Figure E.1) to the rest of the data-set. The IR sizes of these galaxies are compact and similar to other galaxies which are detected. The infrared characteristics as well as example images of these galaxies is discussed in Appendix.

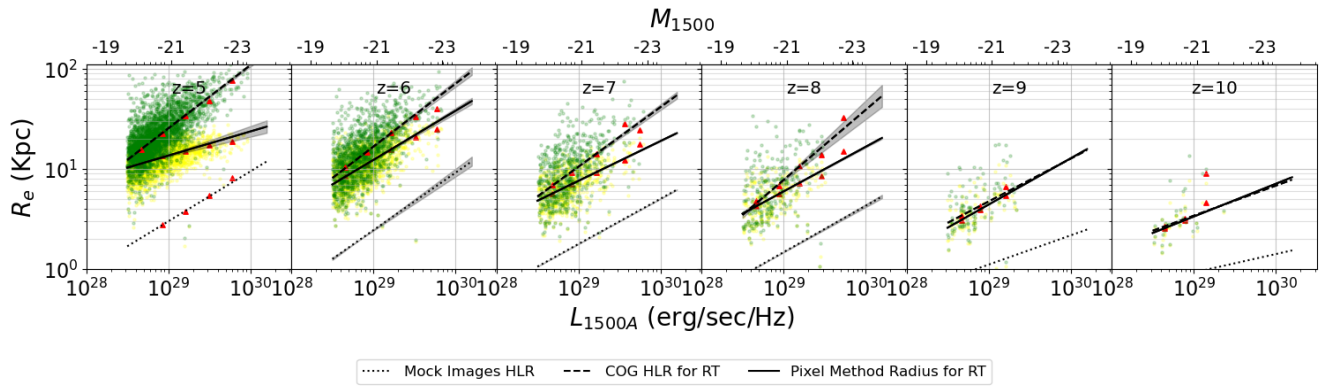


**Fig. D.1.** Luminosity size relation evaluated at different redshifts is shown above. The y-axis shows the UV 1500 Å sizes in kpc and the x-axis shows luminosity at the same wavelength. The green scatter shows our sample of galaxies analysed with radiative transfer for Curves of Growth sizes using circular apertures whereas the yellow scatter shows the sizes for non-parametric Pixel Method as presented in [FLARES IV](#).

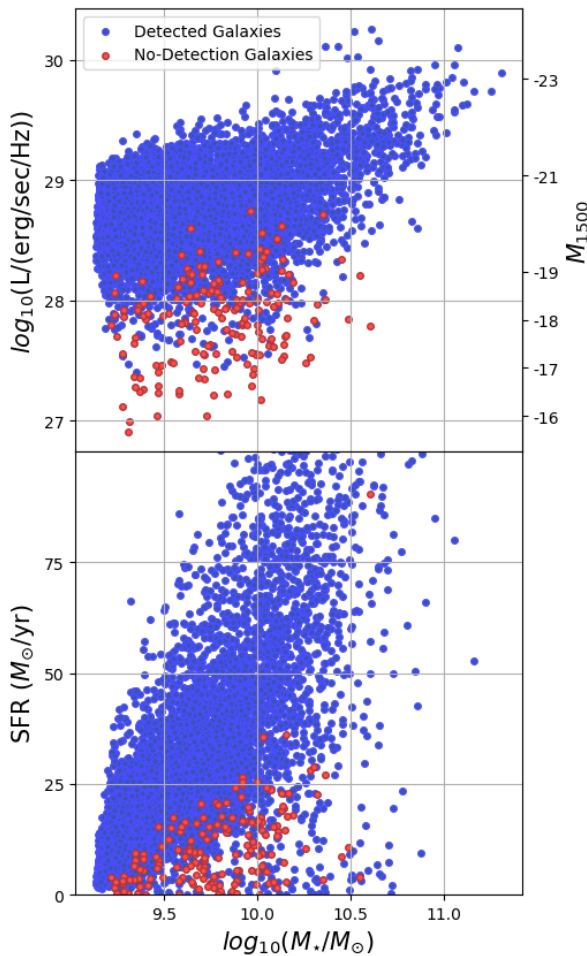


**Fig. E.1.** **Upper panel:** FUV luminosities (y-axis) are plotted against their respective Stellar Masses (x-axis). Detected galaxies are shown in blue and non-detections in red, at SNR=5. The scatter is of the whole sample across all redshifts with most non-detections lying at  $z=5,6$ . **Lower Panel:** Similar figure as the upper panel, we now compare SFR (y-axis) of the galaxies detected using mock images and the ones which were not at different Stellar Masses (x-axis) at SNR=5. Detected galaxies are shown in blue and non-detections in red.

The galaxies which are not detected in UV spectrum, as discussed earlier, have a comparatively lower SFR compared to the general population and they have a low luminosity detected at

1500 Å, but these galaxies have similar luminosities (to general population) in Infrared signifying older stellar population which is also responsible for the stellar mass being comparable to the general population.

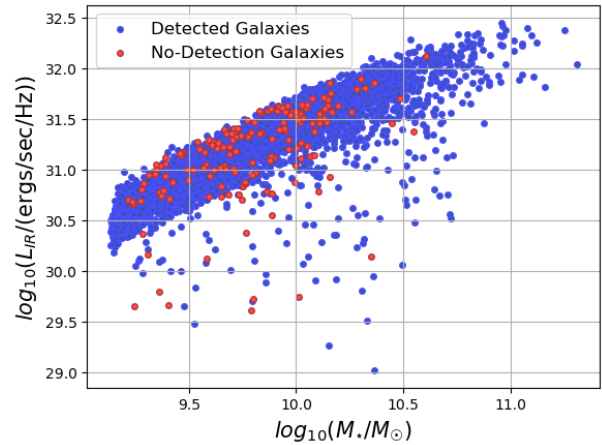


**Fig. E.2.** Infrared Luminosity at 250  $\mu\text{m}$  (y-axis) is plotted against Stellar Mass (x-axis) for the whole population to distinguish infrared properties between FUV detected galaxies against the non detected ones. The non detection so similar spread and pattern to detection.

We also look at the IRX- $\beta$  plot to see if this non-detection can also be due to presence of dust but the galaxies which are not detected are spread across a wide values of IRX and  $\beta$ .

A few sample images of these non detected galaxies with the original, noisy image and then the resultant image when a  $5\sigma$  noise threshold is applied are given in Figures [E.4](#), [E.5](#) and [E.6](#).

## Appendix F: Mock high angular resolution ALMA imaging

Theoretically ALMA can go to very high resolutions, even beyond JWST resolutions, at a lot of galaxy structures will be resolved. The observational time required to achieve these resolutions on a single source remains unjustifiable, but to look at the effects of resolution on ALMA sizes we simulated galaxies' observations with C8 configuration as described in main text. The imaging is presented in Figure [F.1](#).



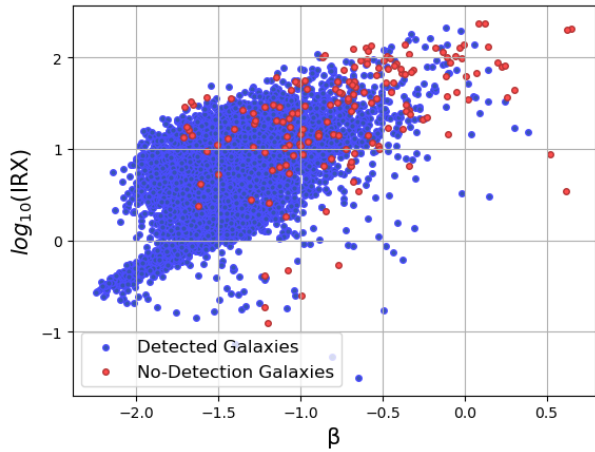


**Fig. E.3.** IRX (y-axis) -  $\beta$  (x-axis) is plotted for the whole sample to investigate the effect of dust between FUV detected galaxies against the non detected ones. No clear pattern for non-detections is established to elude to dust causing non-detections.

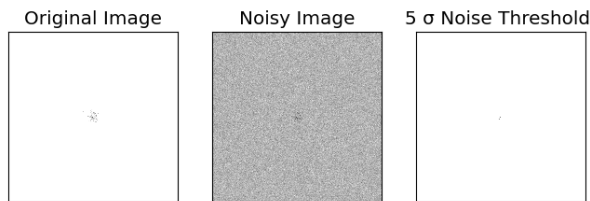


**Fig. E.4.** A sample no-detection galaxy at various stages of image analysis is shown above. The first panel shows the output of radiative transfer, the second panel shows the simulated noisy image with respect to NIRCcam and the last panel shows the residual image after a 5 sigma threshold is applied to remove noise. The final image leads segmentation algorithm finding no credible sources.

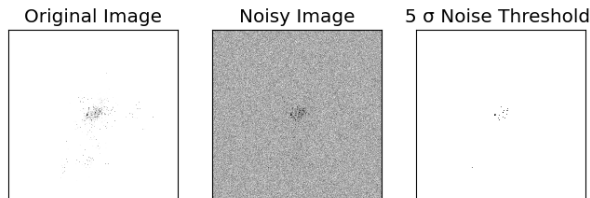


**Fig. E.5.** A sample no-detection galaxy at various stages of image analysis is shown above. The first panel shows the output of radiative transfer, the second panel shows the simulated noisy image with respect to NIRCcam and the last panel shows the residual image after a 5 sigma threshold is applied to remove noise. The final image leads segmentation algorithm finding no credible sources.

## Appendix G: Effect of Noise on ALMA imaging

At low signal to noise ratios in ALMA with very low resolution, noise around the bright centres of galaxies can appear as extended emission. To analyse this effect, in Figure G.1 we plotted the  $158\mu\text{m}$  observed to intrinsic size ratio against observed SNR levels. We see that with decreasing SNR the spread of the size ratio increases towards higher values. This effect is opposite of what is seen for UV emission where the decreasing effect of noise leads to mock *JWST* sizes getting closer to intrinsic sizes.

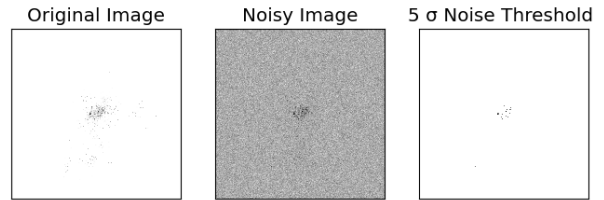


**Fig. E.6.** A sample no-detection galaxy at various stages of image analysis is shown above. The first panel shows the output of radiative transfer, the second panel shows the simulated noisy image with respect to NIRCcam and the last panel shows the residual image after a 5 sigma threshold is applied to remove noise. The final image leads segmentation algorithm finding no credible sources.

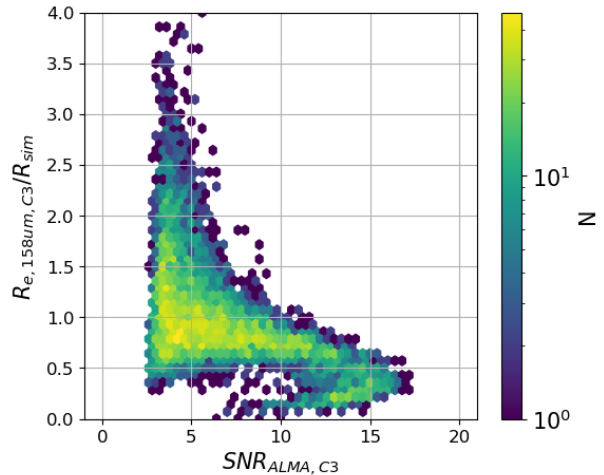


**Fig. G.1.** The figure shows observed to intrinsic size ratio at  $158\mu\text{m}$  (y-axis) plotted against the observed signal to noise ratios (x-axis). The spread of galaxies towards higher size ratios increases with decreasing SNR.

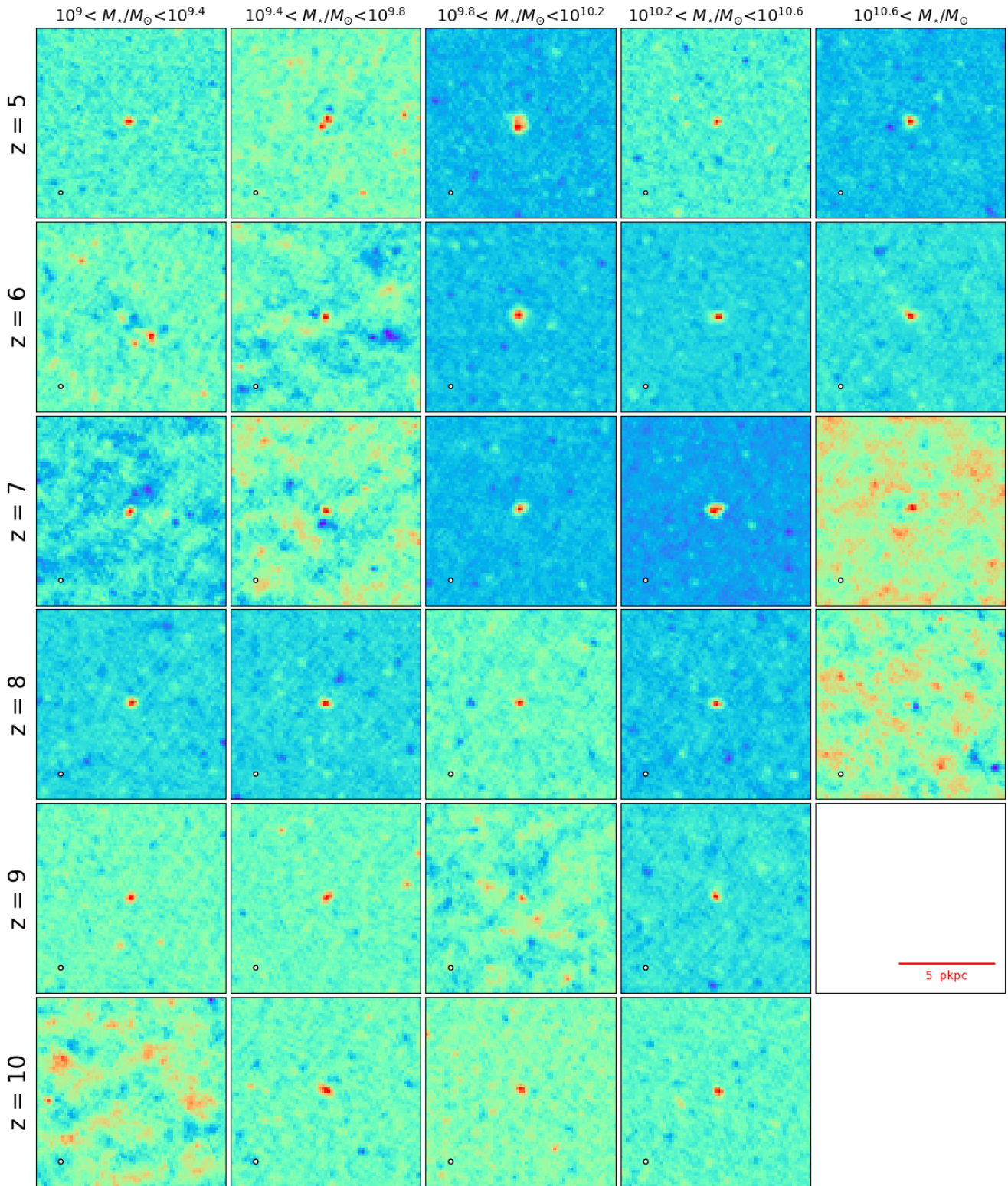


**Fig. F.1.** The figure shows sample galaxies (same galaxies as in Figure 4) at different redshifts and various mass bins as observed by ALMA at  $158 \mu\text{m}$  at very high resolution ( $\approx 0.02''$ ) using C8 configuration. The aperture of the images is 10 pkpc. The beam size is shown by the circle at bottom left corner

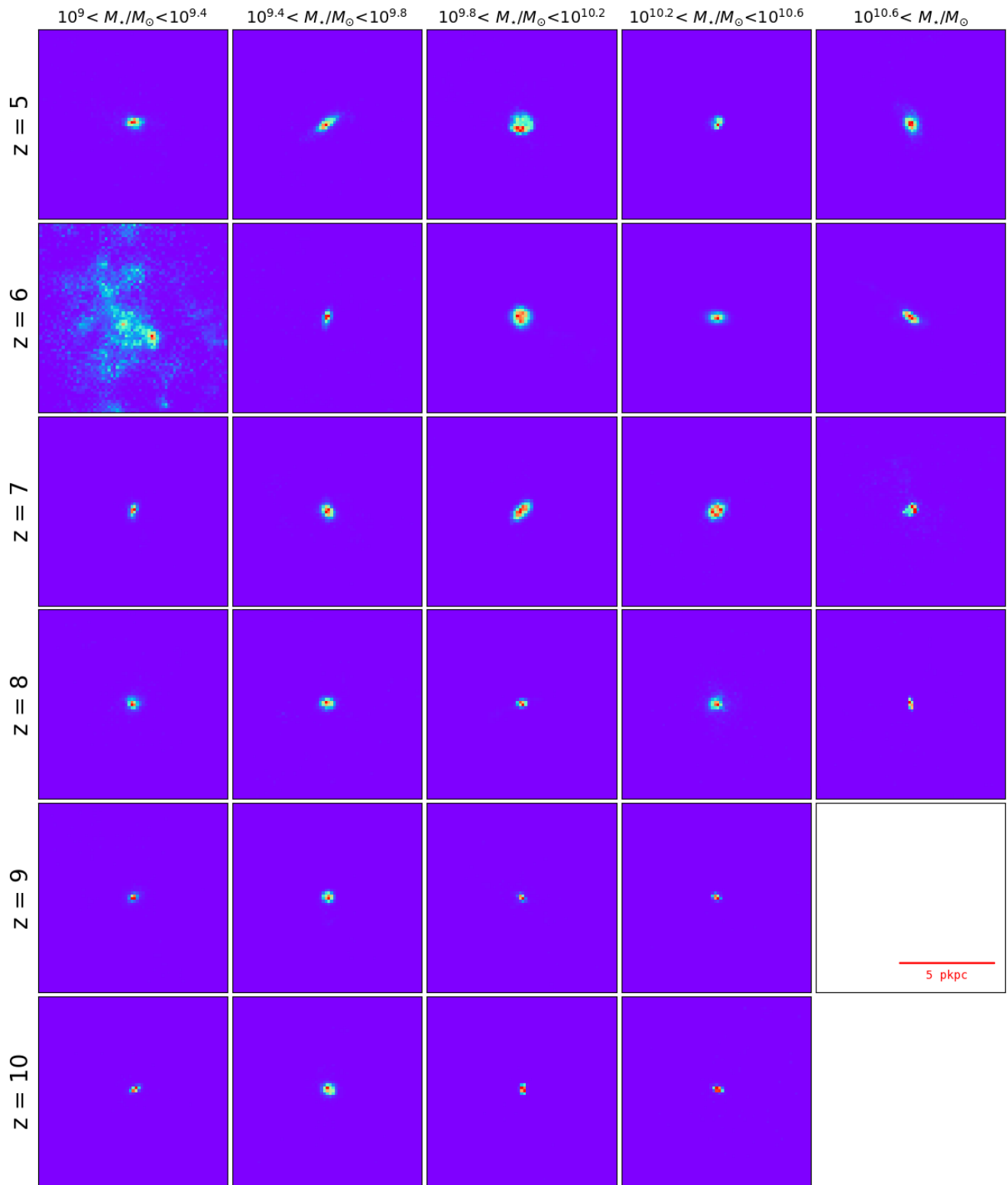


**Fig. F.2.** The figure shows the radiative transfer output at  $158 \mu\text{m}$  of the sample galaxies (same galaxies as in Figure 4). The aperture of the images is 10 pkpc.